

SOLUTION PROCESSABLE THIN FILMS FOR ALL-OXIDE SOLAR CELLS



By

Muhammad Hammad Raza Gardezi

Khizra Maryam

Bilal Hanif

**School of Chemical and Materials Engineering
National University of Sciences and Technology**

2023

SOLUTION PROCESSABLE THIN FILMS FOR ALL-OXIDE SOLAR CELLS



By

(Leader - 00000290357 Muhammad Hammad Raza Gardezi)

(Member 1- 00000309537 Khizra Maryam)

(Member 2- 00000301089 Bilal Hanif)

The thesis is submitted as partial fulfillment of the requirements for
the degree of

BE in Metallurgy and Materials Engineering

Supervisor Name: Dr. M. Talha Masood

School of Chemical and Materials Engineering (SCME)

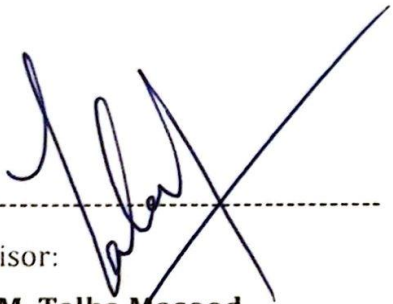
National University of Sciences and Technology (NUST)

June, 2023

CERTIFICATE

This is to certify that work in this thesis has been completed by **Mr. M. Hammad Raza Gardezi, Ms. Khizra Maryam** and **Mr. Bilal Hanif** under the supervision of **Dr. M. Talha Masood** at the school of Chemical and Materials Engineering (SCME), National University of Science and Technology, H-12, Islamabad, Pakistan.

Advisor:



Dr. M. Talha Masood
Department of Materials Engineering
School of Chemical and Materials
Engineering
National University of Sciences and
Technology

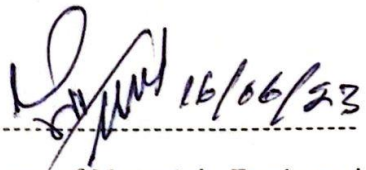
Co-Advisor (if any)



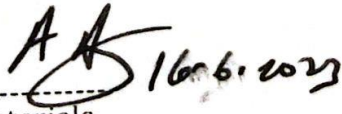
Dr. Sofia Javed
Department of Materials Engineering
School of Chemical and Materials
Engineering
National University of Sciences and
Technology

Submitted Through:

HOD-----


Department of Materials Engineering
School of Chemical and Materials
Engineering
National University of Sciences and
Technology

Principal/Dean -----


School of Chemical and Materials
Engineering
National University of Sciences and
Technology

ABSTRACT

The increasing demand for sustainable energy sources has driven extensive research into solar cells for efficient and environmentally friendly energy conversion. While perovskite-based solar cells have demonstrated promising efficiencies, concerns surrounding their poor stability and potential toxicity due to lead content have shifted the focus towards the development of low-cost, stable, and safe photovoltaic alternatives. In this context, Cu₂O (copper(I) oxide) has emerged as a highly promising photoactive material for solution-processable all-oxide solar cells, offering significant advantages such as low-cost fabrication, environmental friendliness, abundance of constituent elements, and compatibility with low-temperature solution processing techniques.

Cu₂O is a p-type semiconductor with a direct bandgap of approximately 2.0 eV, enabling strong light absorption in the visible range and positioning it as an attractive candidate for photovoltaic applications. Furthermore, Cu₂O exhibits unique properties including high carrier mobility, efficient charge carrier separation, and low recombination rates, which collectively contribute to the overall performance and efficiency of the solar cell device.

This research study primarily focuses on investigating the fabrication methods and parameters used for depositing Cu₂O (copper(I) oxide) thin films. The techniques employed in this study include electrodeposition and Successive Ionic Layer Adsorption and Reaction (SILAR) method. The objective is to explore the influence of these deposition methods and parameters on the properties of the Cu₂O thin films.

TABLE OF CONTENTS

ABSTRACT.....	ii
CHAPTER 1.....	1
INTRODUCTION.....	1
CHAPTER 2.....	4
BACKGROUND.....	4
2.1 Solar spectrum.....	4
2.2 Photovoltaics.....	5
2.2.1 First generation solar cells.....	7
2.2.2 Second generation solar cells.....	8
2.2.3 Third generation solar cells.....	9
2.2.4 Fourth generation solar cells.....	9
2.3 All oxide solar cells.....	10
CHAPTER 3.....	12
LITERATURE	
REVIEW.....	12
3.1 All oxide solar cells.....	12
3.2 UV visible treatment.....	12
3.3 NiO synthesis and characterization.....	13
3.4 Cu ₂ O synthesis and characterization.....	14
CHAPTER 4.....	15
AIMS OF	
STUDY.....	15
4.1 Study 1.....	15
4.2 Study 2.....	15
4.3 Study 3.....	16
CHAPTER 5.....	17
EXPERIMENTATION.....	17
5.1 Materials.....	17
5.1.1 Conductive fluorine -doped tin oxide coated glass.....	17
5.1.2 Hole transport layer.....	17
5.1.3 Photoactive layer.....	17
5.2 Thin film synthesis.....	17

5.2.1	Cleaning of FTO glass slides	17
5.2.2	UV / Ozone treatment.....	18
5.2.3	NiO thin film synthesis.....	18
5.2.4	Cu ₂ O thin film synthesis.....	19
CHAPTER 6.....		22
DENSITY FUNCTIONAL THEORY.....		22
6.1	Background	22
6.1.1	Electronic Density and Energy Functionals:.....	22
6.1.2	Hohenberg-Kohn Theorems:	22
6.1.3	Kohn-Sham Equations:.....	22
6.1.4	Exchange-Correlation Functional:.....	23
6.1.5	Approximations and Density Functional Approximation (DFA):..	23
6.1.6	Computational Implementation:.....	23
6.2	Computation:	25
6.2.1	Nickel Oxide.....	25
6.2.2	Copper (I) Oxide	28
CHAPTER 7.....		31
CHARACTERISATION METHODS.....		31
7.1	Contact Angle Measurement.....	31
7.2	Scanning Electron Microscopy	33
7.3	Energy Dispersive X-Ray Spectroscopy	35
7.4	Optical Profilometry	36
7.5	UV/Vis Spectroscopy.....	38
7.6	RAMAN Spectroscopy.....	40
CHAPTER 8.....		42
RESULTS AND DISCUSSION.....		42
8.1	Effect of UV/Ozone Treatment on the surface wettability of substrate	42
8.2	Analysis of Morphological Characteristics of the hole transport layer	44
8.3	Elemental Analysis of the hole transport layer	46
8.4	Characterization of film thickness for the hole transport layer	47
8.5	Investigation of the optical properties of the photoactive layer	49

8.6 Compositional Analysis of the photoactive layer.....	51
CONCLUSION.....	53
REFERENCES.....	54

LIST OF TABLES

Table 1 Results from Contact Angle measurement.	42
Table 2 Atomic and Weight percentages of the elements obtained from EDX Analysis.....	46
Table 3 Mean Thickness and Mean Roughness of film resulting from variation in dip coating dwell time.....	48

LIST OF FIGURES

Figure 1 Fluctuation of gas prices in year 2021 and onward	2
Figure 2 Description of solar energy and its constituents.....	3
Figure 3 Solar spectrum and its wavelengths.....	5
Figure 4 Basic principle of photovoltaics.	6
Figure 5 Electricity generation principle in photovoltaics.....	7
Figure 6 Solar cell generations and various types.	10
Figure 7 Setup schematic for cyclic voltammetry.....	21
Figure 8 Illustration of the NiO structure used for Optical and Electronic property calculations.	25
Figure 9(a) Electronic Band Structure and Density of States of NiO calculated with GGA using CASTEP.	26
Figure 9(b) Electronic Band Structure and Density of States of NiO calculated with m-GGA using CASTEP.....	27
Figure 10 Optical Absorption Spectrum of NiO calculated with GGA using CASTEP.	27
Figure 11 Illustration of the Cu ₂ O structure used for Optical and Electronic property calculations.	28
Figure 12(a) Electronic Band Structure and Density of States of Cu ₂ O calculated with GGA using CASTEP.	29
Figure 12(b) Electronic Band Structure and Density of States of Cu ₂ O calculated with meta-GGA using CASTEP.	29
Figure 13 Optical Absorption Spectrum of Cu ₂ O calculated with GGA using CASTEP.	30
Figure 14 Schematic showing a liquid droplet making a contact angle θ , with the interfacial energies existing in the system.....	31
Figure 15 Schematic showing the working principle of the Scanning Electron Microscope [46].....	33
Figure 16 Schematic showing the sputtering process required for the preparation non-conductive samples. [47]	35

Figure 17 Schematic showing the working principle of the setup used for Optical Profilometry. [48]	36
Figure 18 Schematic showing the working principle of a UV/Vis Spectrophotometer	38
Figure 19 Schematic representation of the scattering modes in RAMAN Spectroscopy.	40
Figure 20 Plot of Contact Angle against time under UV/Ozone Treatment.....	43
Figure 21(a) Surface Morphology of NiO coated on plain glass slide with a dwell time of 0 minutes.	44
Figure 21(b) Surface Morphology of NiO coated on Plain glass slide with a dwell time of 5 minutes.	44
Figure 22(b) Surface Morphology of NiO coated on FTO substrate with a dwell time of 5 minutes.	45
Figure 22(a) Surface Morphology of NiO coated on FTO substrate with a dwell time of 0 minutes.	45
Figure 23(a) EDX Results for NiO coated on plain glass slide with a dwell time of 0 minutes.	46
Figure 23(b) EDX Results for NiO coated on plain glass slide with a dwell time of 5 minutes.	46
Figure 24(a) Optical Profilometry results for NiO film deposited on plain glass substrate with a dwell time of 0 minutes.	47
Figure 24(b) Optical Profilometry results for NiO film deposited on plain glass substrate with a dwell time of 5 minutes.	47
Figure 25(a) Percentage Transmission of Cu ₂ O films as a function of incident wavelength deposited on plain glass substrate with 20, 40 and 60 SILAR cycles.	49
Figure 25(b) Optical Absorption Spectra for Cu ₂ O films deposited on plain glass substrate with 20, 40 and 60 SILAR cycles.....	49
Figure 26 Optical Absorption Spectrum for Cu ₂ O deposited on FTO glass substrate through electrodeposition.	50
Figure 27 RAMAN Spectroscopy results for Cu ₂ O films deposited on plain glass substrate with 20, 40 and 60 SILAR cycles.....	51

Figure 28 RAMAN Spectroscopy results for Cu_2O deposited on FTO glass
substrate through electrodeposition.52

CHAPTER 1

INTRODUCTION

Due to escalating demand and limited resources, the globe is currently experiencing an energy crisis. Due to the expanding industry and rising use of electronic gadgets, this demand is increasing. The limited supply of fossil fuels is also getting rarer, which raises their costs and reduces their availability. The greenhouse gas carbon dioxide is released into the atmosphere when fossil fuels are burned, which contributes to climate change and global warming. Therefore, it is vital for the globe to cut emissions and switch to more sustainable energy sources. The transition to renewable energy sources like solar, wind, and geothermal is the answer to the global energy dilemma. These energy sources are not only plentiful and sustainable, but they also do not contribute to atmospheric emissions of carbon dioxide. By doing so, emissions will be decreased, and the effects of global warming will be lessened. Additionally, customers can more easily afford renewable energy sources because they are frequently less expensive than their fossil fuel-based counterparts. To create sustainable energy, we must first produce inexpensive solar cells and commercialize them fast enough to meet market needs. [1]

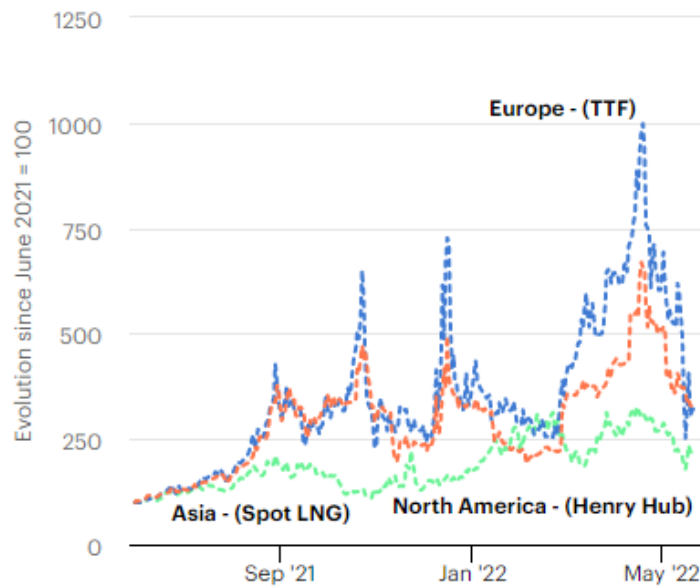


Figure 1 Fluctuation of gas prices in year 2021 and onward

The future of the energy industry will be dominated by solar cells, which are not only proving to be a sustainable and environmentally friendly answer to the present energy issue but can also be a cheap and efficient way to harness solar energy. Here is a quick introduction to solar energy and its use in solar cells.

Solar energy refers to the radiation emitted by the sun that can produce heat energy, accelerating or initiating chemical reactions and producing electricity by solar phenomenon. The total amount of incident solar energy on earth is far more than the current energy needs. This solar energy if harnessed properly can be a salvation of energy crisis. Solar energy is already becoming one of the most attractive energy resources of the 21st century. This is because solar energy is renewable, environmentally friendly and non-polluting energy source which makes it highly sustainable for the future. It can provide a sustainable alternative to conventional energy sources like coal, natural gas and petroleum products that are highly polluting in their nature when consumed in the energy sector.

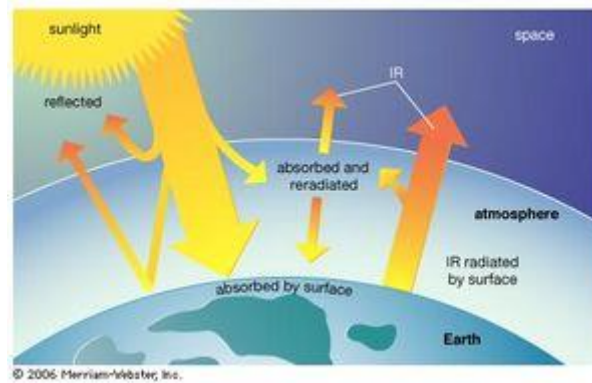


Figure 2 Description of solar energy and its constituents.

The solar energy from sun is an excellent renewable source of energy but it still has its limitations such as,

- The radiation loses intensity due to the large distance of earth with the source.
- Some of the radiations are absorbed by cloud and gases in the atmosphere.
- The materials capable of exploiting solar energy are expensive to manufacture.

For instance, 54% of radiation intensity is lost due to absorption and scattering in the atmosphere. Also, the solar spectrum contains a range of radiation with different energy and efficient conversion of all the radiation to electricity is not possible using conventional solar cells. For the elimination of this problem several new technologies are emerging that allow employment of a greater range of radiation to generate electricity. To reduce the cost as well as to enhance the efficiency of solar cells cost effective techniques to manufacture solar cells are being explored that will be discussed later in this report. [2]

BACKGROUND

As we have already discussed solar energy and its ability to produce electricity now, we will discuss the solar spectrum in detail and how it affects the efficiency of solar devices.

2.1 Solar spectrum

The range of electromagnetic energy that the sun emits, from the ultraviolet to the infrared spectrum, is known as the solar spectrum. It is made up of photons with different wavelengths, which determine the pattern and intensity of the spectrum. It can be explained using solar irradiance or solar radiation. Solar irradiance is the quantity of energy that reaches the Earth's surface, whereas solar radiation is the energy that the sun directly emits.

The ultraviolet (UV), visible, and infrared (IR) spectrum of the sun can be split into three primary categories. Light with a wavelength of less than 400 nanometers (nm) is UV light. The energy of UV photons ranges from about 3 to 5 electron Volts (eV). The visible spectrum spans 400 to 700 nm. Photons in this area have energy between 1.8 and 3 eV. Finally, the IR area consists of light with wavelengths greater than 1000 nm and photon energies ranging from roughly 0.35 eV to 1.8 eV.

The Earth-Sun distance, the angle at which the sun's rays enter the Earth's atmosphere, the weather, and the level of air pollution all have a significant impact on the intensity of the solar spectrum that is received on Earth. sun cells are particularly sensitive to the shape of the sun spectrum and the strength of the radiation because they use photovoltaic technology to convert solar radiation into electricity. Therefore, in order to produce solar cells that function and are as efficient as possible, researchers and engineers working on them must be familiar with the solar spectrum. Hence a knowledge of the solar spectrum is vital before designing a solar cell. [3]

Spectrum of Solar Radiation (Earth)

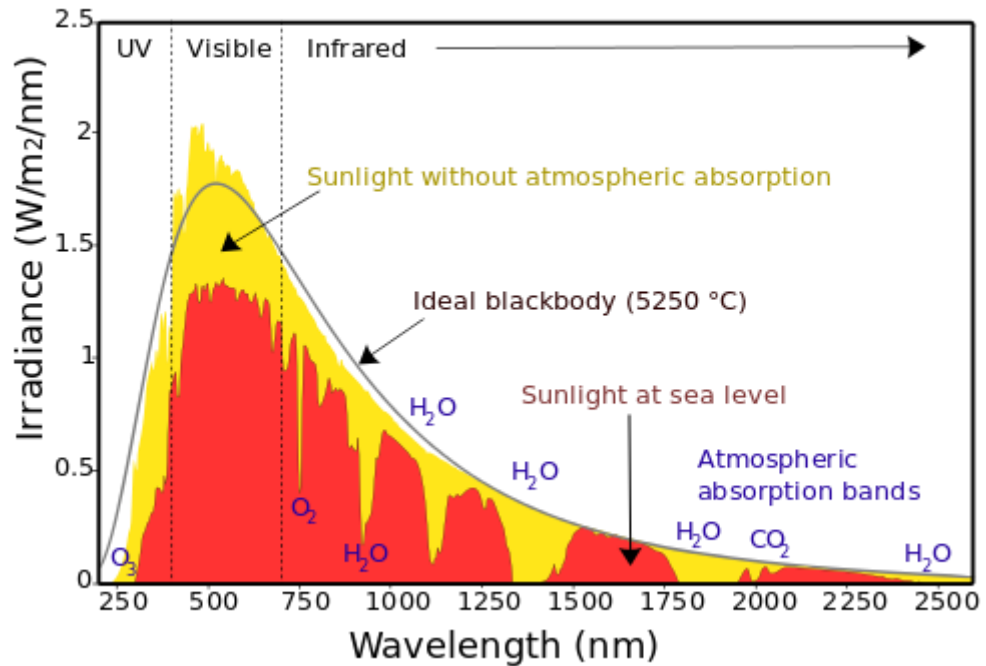


Figure 3 Solar spectrum and its wavelengths.

Given that Earth receives daily sun energy equivalent to nearly 200,000 times the global capacity for generating electricity, solar energy has a tremendous amount of potential. Solar radiation can be transformed into electrical energy or thermal energy (heat); however, the former is simpler to achieve.

2.2 Photovoltaics

Solar cells, often known as photovoltaic cells, are devices that can convert solar energy directly into electricity. When light interacts with the junction between a metal and a semiconductor (such as silicon) or the junction between two separate semiconductors in such cells, a small electric potential is produced. A single solar cell normally only produces two watts of power. However, hundreds or even thousands of kilowatts of electric power can be produced in a solar electric plant or in a big domestic array by joining numerous individual cells together, as in solar-panel arrays.

The solar efficiency of most current photovoltaic cells is about 15-20%, and, because the intensity of solar radiation is low naturally, enormously expensive

assemblies of such cells are required to achieve even moderate volumes of energy.

[4]

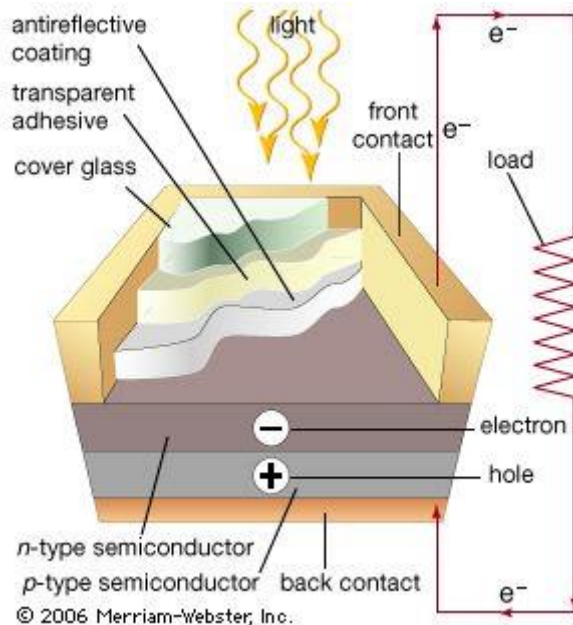


Figure 4 Basic principle of photovoltaics.

Small photovoltaic cells that use natural or artificial light to generate electricity are widely used in low-power applications, such as watches and calculators. Larger units have been used to power weather and communication satellites, remote communications systems, and water pumps. Homeowners and companies can install traditional crystalline silicon panels and cutting-edge thin-film solar cell technologies, such as building-integrated photovoltaics, on their rooftops to supplement or replace the traditional energy supply.

Now as we get an overview of solar energy and its potential use in electricity generation we move forward to the photovoltaic devices and their types.

Solar cells or photovoltaic (PV) cells are non-mechanical devices that use sunshine to generate electricity. Some PV cells can generate electricity from artificial light.

Photons, or solar energy particles, make up sunlight. The energies of these photons, which correspond to the various sun spectrum wavelengths, vary.

A semiconductor is used to construct a PV cell. Photons may bounce off a PV cell, pass through the cell, or be absorbed by the semiconductor material when they hit the cell. Only the photons that are absorbed have the energy needed to produce

electricity. Electrons are ejected from the substance's atoms when the semiconductor material absorbs enough solar energy. [4]

Inside a photovoltaic cell

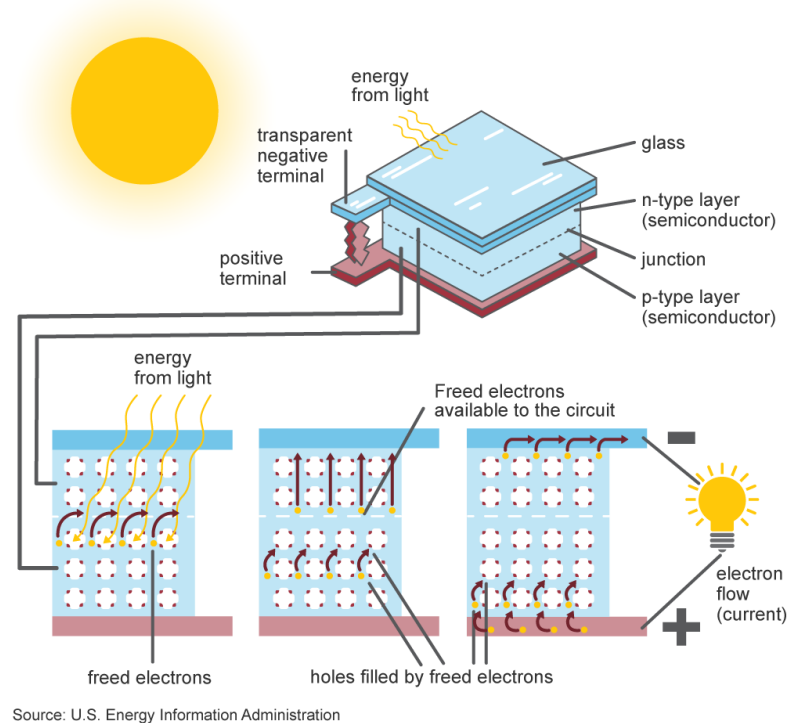


Figure 5 Electricity generation principle in photovoltaics.

A photovoltaic cell's main function is to convert solar radiation from pure light into electrical energy through a process known as the photovoltaic effect. The production of solar cells utilizes a variety of processes, including material modification and cell component photoelectric conversion efficiencies with varying photoelectric conversion rates. Photovoltaic technologies can be categorized into four main generations as a result of the development of numerous non-traditional manufacturing techniques for creating functional solar cells.

2.2.1 First generation solar cells

When Gerald Pearson, Calvin Fuller, and Daryl Chaplin created a silicon photovoltaic cell at Bell Telephone Laboratories in New Jersey in 1954, the photovoltaic technology was formally launched.² A diffused crystalline silicon p-n junction was employed to prepare it. In the semiconductor industry, crystalline silicon is one of the oldest and most widely utilized materials. Still made of crystalline silicon, solar modules are still largely commercially available. The first

generation of solar cells has effectively penetrated the market and has proven to be technically reliable.

Depending on their separate manufacturing process, crystalline solar cells are further divided into single crystalline and poly-crystalline (or multi-crystalline) silicon solar cells. Single crystalline silicon is commonly produced using the Czochralski method. A tiny silicon crystal is dipped into molten silicon in this procedure and dragged out at a very slow but steady speed. As a result, cylinder-shaped single crystal ingots are created, which can then be sliced into wafers for additional processing. In order to create a silicon slab that can be sliced into wafers, molten silicon is cast in blocks to create polycrystalline silicon. Crystalline grains that are randomly orientated are created as a result.

For photovoltaic applications, crystalline silicon must be extremely pure, and producing it requires energy-intensive procedures. Poly-crystalline silicon is produced at a somewhat lower cost than single-crystalline silicon. However, the performance is poor because grain boundaries present a challenge for charge carriers. There are now 27.6% and 23.3% efficiency records for single- and poly-crystalline silicon solar cells, respectively. Due to the indirect band gap semiconductor nature of crystalline silicon, it is employed to best absorb sunlight in the form of relatively thick wafers. Since these wafers are delicate by nature, care must be taken when transporting and installing them. Crystalline silicon cannot be used in thin-film or flexible solar cells, thus. A compound semiconductor called gallium arsenide (GaAs) has a straight band gap, which guarantees both its tremendous light absorption capacity and extremely low non-radiative energy losses. Wafers and thin films can both be made from the material because of its straight band gap, which guarantees adequate light absorption and consequently current generation.

2.2.2 Second generation solar cells

Second generation solar cells, sometimes referred to as thin film solar cells, have been produced in an effort to streamline the production process and lower the cost. In these, the photoactive compounds are typically deposited in thin layers onto glass or flexible substrates. In comparison to silicon wafer-based solar cells,

photo-active thin films for photovoltaic applications require only roughly 5% of the photo-active material. As a result, the price is roughly cut in half as compared to first-generation solar cells.

Amorphous silicon, cadmium telluride, and copper indium gallium di-selenide (CIGS) are among the photoactive components used in second-generation solar cells. However, due to the presence of midgap trap states within its mobility gap, the efficiency of amorphous silicon solar cells has not yet exceeded 14.5%.¹⁸ The thin film photo-active materials can be deposited on a flexible substrate, which reduces the risk of damage during handling.

2.2.3 Third generation solar cells

The Shockley-Queisser limit of 31% to 41% efficiency for single band gap photovoltaics is a barrier that third generation solar cells can overcome. The term emerging thin film photovoltaics also refers to third generation solar cells. The integration of solar panels into building facades or onto automotive surfaces are two examples of expanding the use of solar energy, even though some current generation solar cells may not operate as efficiently as older ones. [5]

2.2.4 Fourth generation solar cells

This generation combines the endurance of "innovative inorganic nanostructures such as metal oxides and metal nanoparticles or organic-based nanomaterials such as graphene, carbon nanotubes, and graphene derivatives" with the poor flexibility or low cost of thin film polymers. [6]

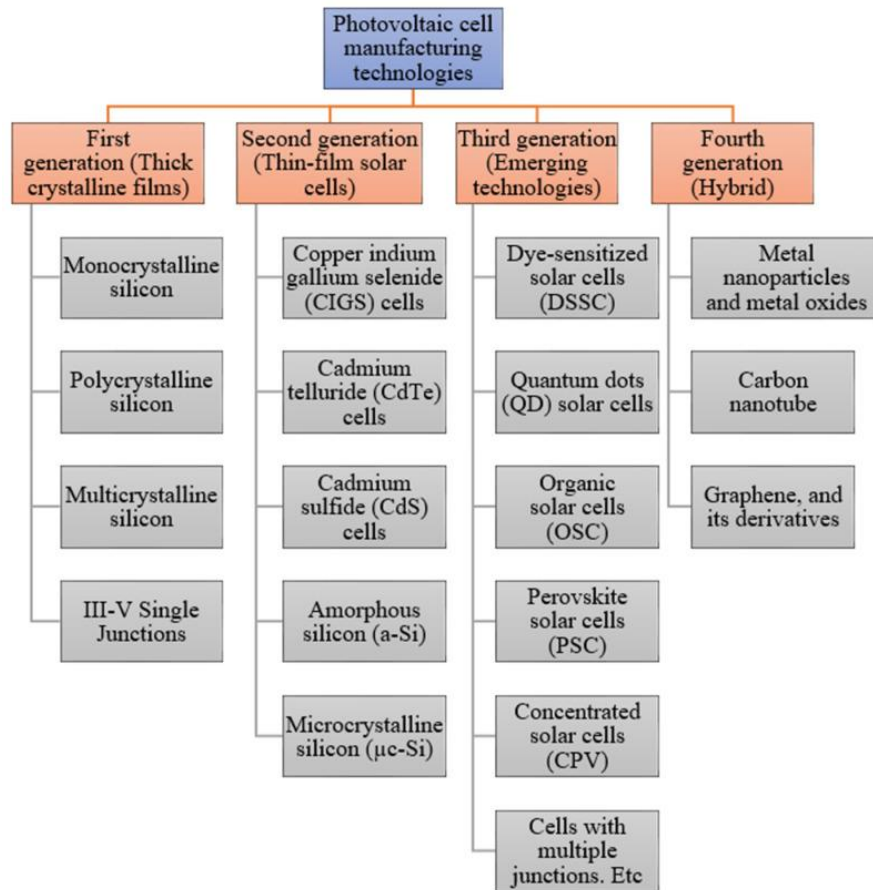


Figure 6 Solar cell generations and various types.

Now narrowing down the scope to our project, our main focus in this study was the optimization of thin films of oxide layers used in all oxide solar cells.

2.3 All oxide solar cells

Photovoltaics (PV) has recently seen the emergence of a new field that focuses on solar cells that are entirely made of metal oxide semiconductors. Due to the chemical stability, nontoxicity, and abundance of numerous metal oxides that may enable manufacture under ambient circumstances, the all-oxide PV strategy is particularly alluring. Metal oxides (MOs) are currently used in a large number of PV cells as electron-transport layers or transparent conducting front electrodes, but they are rarely used as light absorbers. In this perspective, we examine recent advancements in all-oxide photovoltaic systems, which up until recently relied mostly on Cu_2O as an absorber. Additionally, ferroelectric BiFeO_3 -based PV systems, which have recently received a lot of interest, are examined. Oxide solar cells are a type of thin-film photovoltaic device that uses oxide materials as the

active layer. They have gained significant attention in recent years due to their potential to provide a low-cost and sustainable alternative to traditional solar cell technologies. Oxide solar cells can be fabricated using a variety of techniques, including chemical bath deposition, sputtering, and spray pyrolysis. They typically exhibit a low efficiency compared to traditional silicon-based solar cells, with reported power conversion efficiencies ranging from 2-8%. However, their low cost, scalability, and environmental friendliness make them attractive for certain applications, such as off-grid and portable devices. Oxide solar cells are an active area of research, with ongoing efforts to improve their efficiency and stability. Some of the current research directions include exploring new oxide materials, optimizing the device structure, and processing conditions, and developing tandem solar cells that combine different types of oxide materials to increase the overall efficiency. [7]

Copper (I) oxide will be used as the photoactive layer for the photovoltaic device owing to its reported bandgap of 2.0 eV which corresponds to the UV-Visible light region of the electromagnetic spectrum. It does, however, suffer from poor carrier mobility which may be optimized through appropriate annealing temperatures.

Nickel Oxide has been selected as the hole transport layer in the device. NiO acts as an

intrinsically P-Type semiconductor thus allowing it to carry holes away from the absorber layer. Furthermore, it has a reported bandgap of 3.6 eV making it transparent to visible light, hence allowing light to pass through and reach the photoactive layer.

Likewise, Titania (anatase) may be used as an electron extraction layer. The use of this film depends on the performance obtained with the initially planned device structure. Anatase is an intrinsically n-type semiconductor, making it suitable for the application. All of these thin films will be deposited through low-cost processes such as dip coating, at ambient conditions. The back metals contacts will be made via physical vapor deposition technique(s), i.e., thermal evaporation.

LITERATURE REVIEW

3.1 All oxide solar cells

The use of metal oxide thin films in solar cell applications has received a lot of interest. These films were created using a variety of deposition techniques. To improve the design of the material, it is crucial to characterize the properties of films. The photovoltaic characteristics of many types of solar cells made under diverse experimental settings have been compiled in this review. The results showed that metal oxide might be used in solar cell applications as an electron transport layer, an electron conducting medium, an anti-reflecting layer, and a hole transport material. [8]

All-oxide PV cells hold the potential to provide incredibly affordable PV systems. All-oxide photovoltaic cells with an absorber made of Cu_2O , CuO , Co_3O_4 , Fe_2O_3 , and BiFeO_3 have so far been developed. Low conversion efficiencies are attained with the other MO absorbers, despite the Cu_2O system having reported promising conversion efficiencies. We anticipate realizing thin film PV cells with new MOs that perform similarly to current thin film technologies but at significantly lower fabrication costs. Other fields of research and development, including the pharmaceutical industry, biology and chemistry, as well as solid-state physics, have found great success with combinatorial synthesis, large-throughput characterization, and computational data processing techniques. [9]

3.2 UV visible treatment

The sol-gel dip-coating process was successful in producing silica films. When compared to a pure glass substrate, the transmittance spectra of changed silica films caused by UV/Ozone treatment exhibit no change. Complete water spreading was achieved for UV Ozone exposure times of up to 20 min, according to surface wettability of silica films determined by contact angle and AFM picture. Results in general showed that the superhydrophilicity property on modified silica film was enhanced due to strong Si-OH surface bonding, clean surface morphologies, and wicking effect following UV/Ozone treatment. [10]

3.3 NiO synthesis and characterization

Nickel nitrate hexahydrate and sodium hydroxide were used in the sol-gel process to successfully create nanostructured NiO particles. The XRD results show that the synthesized particles are nanocrystalline, and the crystallite size at calcination temperature (600 °C) is determined to be 16.26 nm. The FTIR spectrum showed that NiO nanoparticles had formed. Diffuse reflection spectroscopy was used to measure the optical band gap of NiO nanoparticles, which was found to be 4.47 eV. The absorption band edge was determined to be 277.27 nm, and photoluminescence spectroscopy verified that nickel oxide is a wide band gap semiconductor. [11]

A nickel oxide thin film was successfully produced using the sol-gel technique. According to the XRD pattern, the NiO thin film displays a respectable nanocrystalline cubic structure. To examine surface morphology, the FESEM was employed. It was discovered that the desired characteristics of nickel oxide thin films produced by the dip coating technique were necessary for their application in energy-efficient transparent heat mirror multilayer technologies. They had ferociously invaded their smooth and dense surfaces, which showed sub-nanoscale surface roughness and directed crystalline development. Optically, NiO thin films outperform other thin films. The high broad bandgap of the NiO thin films is 3.78 eV. NiO multilayers are used to create transparent heat mirrors with thicknesses of 107 nm and 103 nm. Chemical depth profiling was used to find that there were many layers of NiO present. The cause of this was discovered to be the porous character of nickel oxide thin films. The heat mirror displayed a maximum transmittance of 70% at 554 nm. The performance of the heat mirror was assessed using the visible-to-solar transmittance.

The combined infrared reflectance was 77%. This figure is appropriate given the range of temperatures. These results point to a regular structure as well as both regular and irregular shapes. That has been demonstrated via optical absorption experiments. PL increased when the annealing temperature was lowered. The results showed low absorbance in the visible and infrared bands and an energy difference of 3.7 eV. [12]

3.4 Cu₂O synthesis and characterization

Cu₂O and CuO thin films have been created by us using the SILAR technique. We have completely characterized the thin films produced using a non-vacuum process and ambient conditions. Cu₂O layer formation also took place at ambient temperature. We have created NiO/Cu₂O/ZnO/SnO₂ and NiO/CuO/ ZnO/SnO₂ heterojunction solar cells using such thin films of p-type Cu₂O and a layer of n-type SnO₂. NiO was employed as a hole-transporting layer as well as an electron-blocking layer, while ZnO served as a buffer layer to prevent chemical changes from happening at the interface between p- and n-type layers. The power conversion efficiency of the devices based on the oxide materials frequently exceeded 1%. [13]

The sequential ionic adsorption and reaction technique, followed by vacuum and air annealing processes, has been effectively used to make copper oxide amorphous and crystalline films with good quality and clarity. Nano-sized crystallites and nano-spherical grains define the annealed films. The following three annealing temperature zones provide a summary of the bandgap depending on the annealing temperature.

1. In the 300–373 K temperature range. Due to defect redistribution in amorphous copper oxide films with a Cu₂O-predominant phase, the band gap was slightly raised from 2.3 to 2.4 eV.
2. In the 373-673K temperature range. The band gap gradually shrunk as a result of annealing-induced crystallization, and nanostructured films with a dominating Cu₂O crystalline phase were created, Between 673 and 823 K, a higher temperature range. [14]

AIMS OF STUDY

In this thesis, NiO and Cu₂O thin films were studied as hole selective layer and photoactive layer for All Oxide Solar Cells respectively. Thin films of NiO and Cu₂O were synthesized using Dip Coating and Successive Ionic Layer Adsorption and Reaction respectively. For this thesis, three different studies were conducted on NiO and Cu₂O, which are schematically discussed below.

Study 1
Synthesis of the solution
for photoactive layer and
hole selective layer

Study 2
Surface activation of
FTO through
UV / Ozone treatment

Study 3
Optimization
of solution
processable
thin films for
AOSCs

4.1 Study 1

The synthesis of the solution for the photoactive layer (Cu₂O) and hole selective layer (NiO) in metal oxide solar cells typically involves specific procedures and reagents. It's important to note that the specific synthesis methods and conditions may vary depending on the desired properties, film thickness, and the equipment available.

4.2 Study 2

Both UV and ozone treatments are effective in activating the FTO surface by modifying its surface chemistry and increasing its surface energy. These processes increase the adherence of later layers and boost the efficiency of devices like solar cells. Depending on the equipment, substrate, and application requirements, the precise treatment parameters, such as UV intensity, exposure time, ozone concentration, and exposure duration, may change.

4.3 Study 3

Optimization of solution processable thin films for all oxide solar cells is done through making changes in solution formulation, deposition techniques, using pretreatments and annealing, and wettability.

EXPERIMENTATION**5.1 Materials****5.1.1 Conductive fluorine -doped tin oxide coated glass.****5.1.2 Hole transport layer**

- a. Precursor: Nickel acetate tetrahydrate
- b. Solvents: Ethanol, Acetic acid

5.1.3 Photoactive layer

- a. Precursor: CuCl_2 (cationic), H_2O_2 (anionic)
- b. Solvents: Methanol
- c. Stabilizer: NH_4OH

5.2 Thin film synthesis

In this project, the dense NiO and Cu_2O were synthesized. First, we focused on the hole selective layer of NiO. It was deposited using dip coating method in which FTO glass was dipped in transparent NiO solution. Then, we synthesized Cu_2O using Successive Ionic Layer Adsorption and Reaction (SILAR) method. Before doing coatings through different methods, FTO glass slides were cleaned properly followed by the UV/Ozone treatment.

5.2.1 Cleaning of FTO glass slides

Cleaning of glass slides is necessary because they often have contaminants such as dust, oil, and other particles that can interfere with the formation of a uniform and smooth film. These contaminants can also negatively affect the wettability of the glass slide, which is critical for the dip coating process. In addition, the presence of contaminants on the glass slide can lead to variations in film thickness, surface roughness, and other properties, which can ultimately impact the performance of the resulting device or application [15].

The slides were cleaned in a sonication bath for 10-15 minutes each with

- a. DI water

- b. Acetone
- c. Ethanol

in the given order. The slides were subsequently dried in the drying oven.

5.2.2 UV / Ozone treatment

UV/Ozone treatment, also known as ultraviolet/ozone cleaning or UV/ozone surface modification, is a surface treatment technique that uses ultraviolet (UV) radiation and ozone to clean, activate, or modify the surface of a material. During the process, a substrate is exposed to UV radiation and ozone in a special chamber. The UV radiation breaks down the oxygen molecules (O_2) in the air to form reactive oxygen species (ROS), which then react with other molecules on the surface of the substrate to form a thin layer of oxygen-containing functional groups. The ozone also reacts with the surface of the substrate, creating more oxygen-containing functional groups [16].

The glass slides after cleaning were placed in the UV/Ozone treatment chamber for a period of 60 minutes to increase surface wettability.

5.2.3 NiO thin film synthesis

NiO thin films were synthesized using dip coating method. Dip coating is a process used to deposit a thin film onto a substrate. In this process, the substrate is dipped into a solution containing the material to be deposited, and then withdrawn at a controlled rate. As the substrate is withdrawn, the solution forms a thin layer on its surface, which then dries to form a solid film. The thickness of the resulting film can be controlled by varying the withdrawal rate, the solution concentration, and other process parameters. Dip coating is a relatively simple and cost-effective technique for depositing thin films on a variety of substrates and is commonly used in the production of a range of materials and devices, including solar cells, sensors, and coatings for corrosion protection [19].

It consists of four steps including,

a. Dwelling

Dwelling is the dipping of substrate into the solution with a predefined speed and then leaving the substrate in the solution to promote further nucleation of the coating.

b. Withdrawal

Withdrawal is the process of withdrawing the substrate out of the solution after proper dwell time.

c. Drying

After withdrawing the substrate, the coated film is dried either using a blow drier or by placing it in a furnace at 100^o C for 30-60 minutes.

d. Curing

After drying the curing process of thin films is done to calcine the coating so that it becomes compact and does not deteriorate.

For our experimentations the oxide coatings were deposited on the surface treated glass slides, with a withdrawal speed of 85mm/s using the following dwell times.

- 0 minutes (dipped and withdrawn)
- 5 minutes

Then substrates are dried on hot plate for 10 minutes and then annealed in the furnace for four hours at 450°C.

5.2.4 Cu₂O thin film synthesis

5.2.4.1 SILAR Method

Cu₂O thin films were synthesized using different precursors, The difference there was of initial precursors. Copper sulphate pentahydrate or copper chloride dihydrate can be used as cationic precursor while H₂O₂ was anionic precursor in both cases.

Highly pure copper (II) chloride dihydrate (CuCl₂ · 2H₂O), ammonium hydroxide (NH₄OH), and hydrogen peroxide (H₂O₂) were employed as copper precursors, complexing agents, and oxidizing agents, respectively, to create thin films of Cu₂O using the SILAR method.

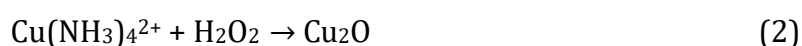
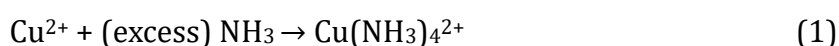
Methodology 1

Methanol that has been dehydrated served as a solvent for the creation of the film. The copper salt (341 mg) was dissolved in 0.1 M of methanol to create the cationic precursor. At pH 11.8 the solution was complexed with 25% NH₄OH. As a result, the copper salt homogenous solution changed from a light green hue to a deep blue one. A 1% H₂O₂ solution (0.2 mL) diluted in 20 mL of methanol was used for the oxidation process. In the SILAR method, dehydrated methanol was used as a rinse solution in between each immersion.

For the growth of Cu₂O films, the four steps below were followed in that order:

1. To allow for the copper ion adsorption, substrates were vertically dipped at a rate of 400 mm/min in the cationic (copper) precursor.
2. To get rid of loosely bonded ions, the substrates were dipped in methanol held at the same speed in another beaker. After some time, they dried using the airflow.
3. To oxidize the copper ions that had been adsorbed, the substrates were next submerged in an H₂O₂ solution for 10 s. The presence of the oxidation process may be implied by the formation of bubbles.
4. In a different beaker, the substrates containing Cu₂O were rinsed in methanol before undergoing the same drying procedure.

The reactions that proceeded can be written as:



To produce Cu₂O thin films of the necessary thickness, the steps were organized in that order. Therefore, the technique used to create Cu₂O thin films continued to be carried out at ambient temperature. The Cu₂O layer was annealed at 450 °C for 30 min to transform Cu₂O thin films to CuO. During the annealing procedure, a definite shift in the film's color could be seen.

Methodology 2

The sodium thiosulfate (Na₂S₂O₃, Merck) solution and the copper sulphate pentahydrate (CuSO₄·5H₂O, Merck) solution were combined to create a cationic 1 M colorless copper thiosulfate [Cu(S₂O₃)]- complex solution, which was then used to create the Cu₂O thin film. The ionic solution employed was 2 M sodium hydroxide (NaOH, Merck). A temperature-controlled heater maintained the ionic solution's consistent temperature at 70 °C. The cleanliness of the substrates is one of the essential conditions for a good grade film. The quality and characteristics of the thin film are influenced by how clean the substrate is. In this work, soda lime glass substrates with dimensions of 76 mm 26 mm x 1 mm were employed. The substrates underwent rigorous cleaning. Because soda lime glasses transmit visible light very effectively and have a high temperature tolerance that can

withstand up to 600 °C, they were chosen as a substrate because they are ideal for optical applications. The glasses were first given a 10-minute soak in chromic acid before being rinsed under running water. They were then rinsed with tap water and cleaned with detergent water. After that, they were submerged in deionized water for 10 minutes. After 15 minutes in 99.9% pure ethyl alcohol, they were washed with water. Finally, they were dried in the furnace for an hour at 100 °C. The cleaned glass substrate was first vertically lowered for 2 seconds into a 70 °C sodium hydroxide solution (NaOH). The substrate shifted from pale yellow to brown as the number of SILAR cycles increased. In this study, chemical processes that took place throughout the deposition procedure created the Cu₂O thin layer. [50]

5.2.4.2 Electrodeposition

On a glass substrate coated with FTO, Cu₂O thin films were electrodeposited using a conventional three electrode setup. We employed a saturated calomel electrode (SCE) as the reference electrode, an FTO of 1 x 1.3 cm as the working electrode (WE), and platinum mesh as the counter electrode (CE). The substrates were ultrasonically cleaned in acetone, ethanol, and then rinsed in distilled water for 15 minutes prior to the deposition. The aqueous solution used to create the thin films contained 0.4M copper sulphate (CuSO₄·5H₂O), 3M lactic acid, and was pH-adjusted to 9 using sodium hydroxide (NaOH) while the bath temperature was kept at 60°C. Using a Voltalab PGZ 301 with Volta master 4 software, the temperature dies were carried out during the electrodeposition. [51]

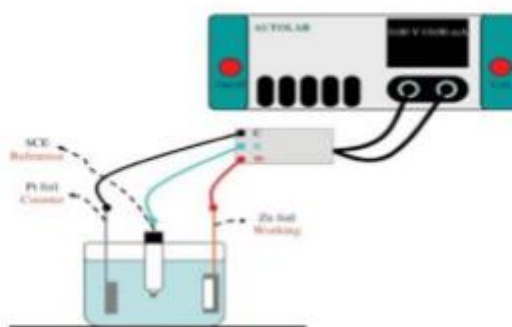


Figure 7 Setup schematic for cyclic voltammetry

DENSITY FUNCTIONAL THEORY

6.1 Background

6.1.1 Electronic Density and Energy Functionals:

At the heart of DFT lies the concept of the electron density ($\rho(r)$), which is defined as the probability density of finding an electron at a given position in space. Instead of describing the wavefunctions of individual electrons, DFT focuses on the electron density as the fundamental quantity. The total energy (E) of a system can be expressed as a functional of the electron density ($E[\rho]$), wherein the ground-state energy is minimized with respect to variations in the electron density. [20]

6.1.2 Hohenberg-Kohn Theorems:

The foundational principles of DFT are encapsulated in the Hohenberg-Kohn theorems. The first Hohenberg-Kohn theorem states that the ground-state electron density uniquely determines the external potential ($V(r)$) in a system. This implies that all observable properties can be expressed as functionals of the electron density.

$$V(r) = V[\rho(r)] \tag{3}$$

The second Hohenberg-Kohn theorem establishes the existence of a universal energy functional ($E[\rho]$) that yields the true ground-state energy when minimized with respect to the electron density. [20]

$$E[\rho] = \min\{\psi \rightarrow \rho(r)\} [T[\rho] + V[\rho] + J[\rho] + E_{xc}[\rho]] \tag{4}$$

6.1.3 Kohn-Sham Equations:

To practically implement DFT, the Kohn-Sham formalism was introduced. The Kohn-Sham equations are a set of equations derived from the Hohenberg-Kohn theorems, which involve auxiliary non-interacting electrons in an effective potential. These equations resemble the form of the Schrödinger equation, with an additional term accounting for the exchange-correlation effects. [20]

$$\left[-\left(\frac{\hbar^2}{2m}\right)\nabla^2 + V_{eff(r)}\right]\psi_i(r) = \epsilon_i\psi_i(r) \tag{5}$$

$$V_{eff(r)} = V_{ext(r)} + V_H(r) + V_{xc(r)} \text{ [Effective Potential]} \tag{6}$$

6.1.4 Exchange-Correlation Functional:

The exchange-correlation functional ($E_{xc}[\rho]$) accounts for the many-body effects and correlations among electrons that are not explicitly included in the Kohn-Sham equations. It incorporates both the exchange (due to the Pauli exclusion principle) and correlation (arising from electron-electron interactions) contributions to the total energy. The form of the exchange-correlation functional remains a topic of research and approximations, and a variety of functionals have been developed with varying accuracy and computational efficiency. [20]

$$E_{xc} = \int \rho(\mathbf{r}) \varepsilon_{xc}[\rho(\mathbf{r})] d\mathbf{r} \quad (7)$$

6.1.5 Approximations and Density Functional Approximation (DFA):

Due to the complexity of the exchange-correlation functional, practical calculations often employ approximations to make DFT computationally tractable. One such approximation is the Local Density Approximation (LDA), which assumes that the exchange-correlation energy per electron is uniform throughout space. Another commonly used approximation is the Generalized Gradient Approximation (GGA), which considers the density gradient to improve the accuracy of the functional. More advanced approximations, such as hybrid functionals and meta-GGAs, incorporate additional information to better describe specific electronic and structural properties. [20]

$$E_{xc} = \int \rho(\mathbf{r}) \varepsilon_{xc}[\rho(\mathbf{r}),] d\mathbf{r} \approx \int \rho(\mathbf{r}) \varepsilon_{xc}[\rho] d\mathbf{r} \quad [\text{LDA}] \quad (8)$$

$$E_{xc} = \int \rho(\mathbf{r}) \varepsilon_{xc}[\rho(\mathbf{r}), \nabla \rho(\mathbf{r})] d\mathbf{r} \quad [\text{GGA}] \quad (9)$$

6.1.6 Computational Implementation:

Implementing DFT involves solving the Kohn-Sham equations self-consistently, iteratively updating the electron density until convergence is achieved. Numerical techniques, such as basis sets or plane wave expansions, are used to represent the wavefunctions and electron density.

For this thesis we used CASTEP (Computer Aided Software for Theoretical Chemistry) which is a widely used program that employs Density Functional Theory (DFT) to simulate and predict material properties. [20]

Calculation Workflow in CASTEP:

- **Atomic Structure Setup:**

The first step in a CASTEP calculation is to define the atomic structure of the material of interest. This includes specifying the positions of atoms in the unit cell, lattice parameters, and any symmetry constraints. [21]
- **Pseudopotential Generation:**

CASTEP employs pseudopotentials to represent the interaction between valence electrons and atomic cores. Pseudopotentials are generated based on the chosen exchange-correlation functional and the properties of the specific elements present in the material. [21]
- **K-Point Sampling:**

To calculate properties in periodic systems, CASTEP employs a discretization scheme known as k-point sampling. K-points represent specific points in reciprocal space and are used to integrate the electronic wavefunctions and Brillouin zone. [21]
- **Electronic Structure Calculation:**

CASTEP solves the Kohn-Sham equations iteratively to determine the electronic structure of the material. This involves self-consistently updating the electron density until convergence is achieved. The chosen exchange-correlation functional, such as LDA or GGA, is used to approximate the exchange and correlation contributions to the total energy. [21]
- **Property Calculation:**

Once the electronic structure is obtained, CASTEP can calculate various material properties. These properties include:

 - i. **Total Energy:** The total energy of the system, including both the electronic and ionic contributions.
 - ii. **Forces and Stress:** The forces acting on each atom, providing information about structural stability and mechanical properties. Stress calculations enable the investigation of mechanical responses to external forces.
 - iii. **Band Structure:** The energy levels and allowed electronic states in the material, providing insights into its electronic properties, such as the presence of band gaps and conducting behaviour.

- iv. **Density of States (DOS):** The distribution of electronic energy levels, revealing information about the energy levels available to electrons in the material.
- v. **Vibrational Frequencies:** The vibrational modes and corresponding frequencies, which allow the analysis of lattice dynamics and phonon properties.
- vi. **Optical Properties:** CASTEP can calculate optical spectra, including absorption coefficients, refractive indices, and dielectric functions, enabling the study of light-matter interactions.
- vii. **Reaction Energies:** CASTEP can also investigate reaction energies and transition states, providing insights into chemical reactions and catalytic processes.

6.2 Computation:

6.2.1 Nickel Oxide

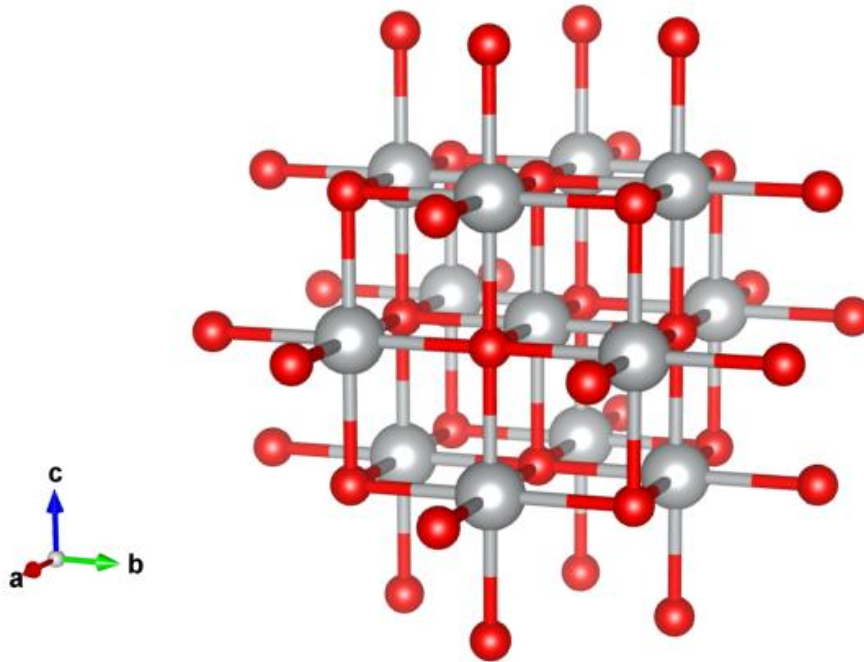


Figure 8 Illustration of the NiO structure used for Optical and Electronic property calculations.

During the computational procedure involving geometry optimization and electronic structure calculation, the Perdew-Burke-Ernzerhof (PBE) functional, which is a generalized gradient approximation (GGA) in density functional theory

(DFT), was employed. Given that Nickel Oxide (NiO) primarily consists of lighter elements, the influence of spin-orbit coupling (SOC) on the band structure was disregarded in the calculation.

To discretise the Brillouin zone, a k-point grid with dimensions of $5 \times 5 \times 5$ was utilized for the NiO system. The plane-wave cutoff energy, which determines the accuracy of the expansion of electronic wave functions, was set to 300 eV for the GGA calculation whereas for m-GGA calculation it was set to 489 eV.

For the electronic configuration of the oxygen (O) atoms, a pseudo-atomic calculation was performed, considering the $2s^2 2p^4$ electronic configuration. Similarly, a pseudo-atomic calculation was carried out for the nickel (Ni) atoms, taking into account the $3d^8 4s^2$ electronic configuration. These pseudopotential-based calculations effectively model the behaviour of the valence electrons while reducing the computational complexity associated with explicitly including the core electrons.

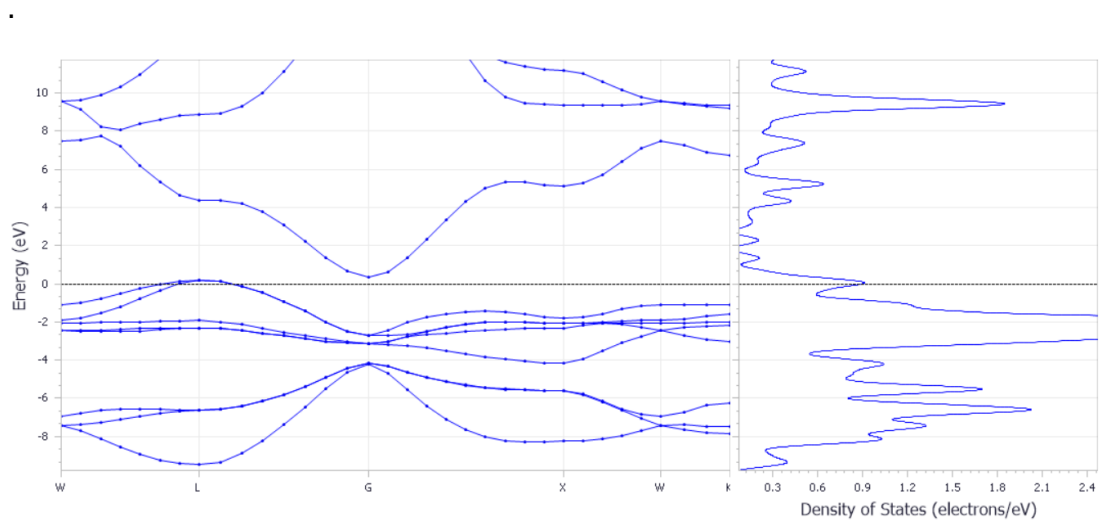


Figure 9(a) Electronic Band Structure and Density of States of NiO calculated with GGA using CASTEP.

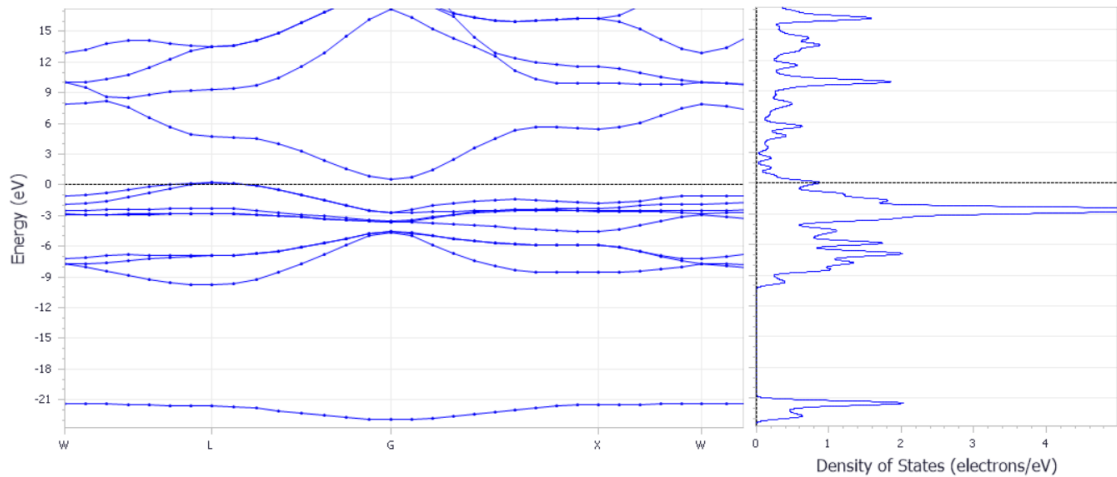


Figure 9(b) Electronic Band Structure and Density of States of NiO calculated with m-GGA using CASTEP.

A generalized gradient approximation (GGA) was employed in the density functional theory (DFT) calculation to determine the electronic band structure of Nickel Oxide (NiO). The calculated theoretical bandgap obtained from this calculation was found to be 3 eV. However, it should be noted that this value underestimates the experimental range of 3.6 eV to 4.0 eV [43], which is widely accepted as the actual bandgap of NiO. The calculation was repeated with meta-generalized gradient approximation (m-GGA), the resulting electronic band structure provided a bandgap value of 3.25 eV.

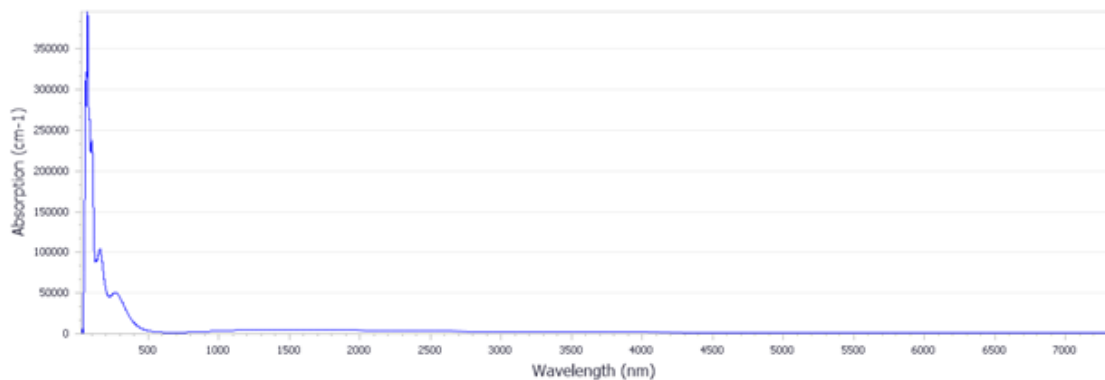


Figure 10 Optical Absorption Spectrum of NiO calculated with GGA using CASTEP.

The absorption characteristics of Nickel Oxide indicate that its absorption is nearly negligible for wavelengths exceeding 500 nm. Moreover, its absorption is generally very low in the UV/visible region, enabling photons within this wavelength range

to pass through the material without being absorbed. This particular property renders Nickel Oxide suitable for application as a hole transport layer.

Nickel Oxide's limited absorption in the UV/visible region stems from its large bandgap energy, which defines the minimum energy required for electron excitation from the valence band to the conduction band.

6.2.2 Copper (I) Oxide

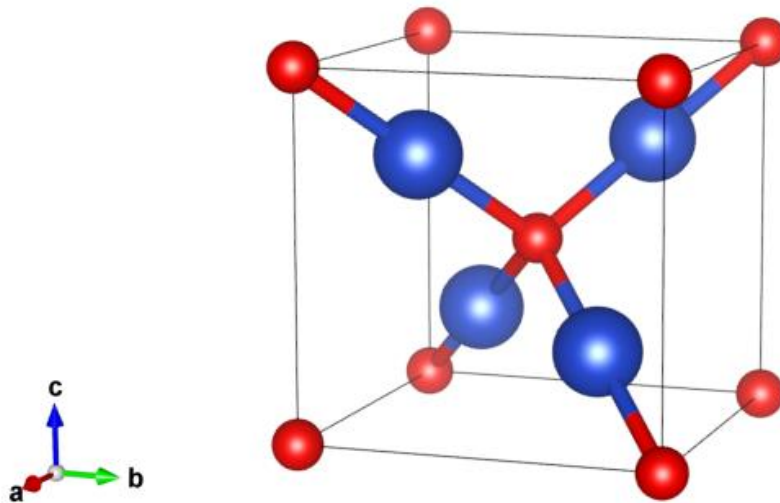


Figure 11 Illustration of the Cu₂O structure used for Optical and Electronic property calculations.

During the computational process involving geometry optimization and electronic structure calculation, the Perdew-Burke-Ernzerhof (PBE) functional with the generalized gradient approximation (GGA) was employed. In the case of Cu₂O, which comprises lighter elements, the consideration of the spin-orbit coupling (SOC) effect was omitted in the band structure calculation.

A k-point grid with dimensions of $4 \times 4 \times 4$ was utilized for the Cu₂O system. The plane-wave cutoff energy, which determines the accuracy of the expansion of electronic wave functions, was set to 489 eV for both GGA and m-GGA calculations. Regarding the electronic configuration, a pseudo-atomic calculation was conducted for the oxygen (O) atoms, considering the electronic configuration of $2s^2 2p^4$. Similarly, a pseudo-atomic calculation was performed for the copper (Cu)

atoms, considering the electronic configuration of $3d^{10} 4s^1$. These pseudo-atomic calculations effectively capture the behaviour of the valence electrons while reducing the computational complexity associated with explicitly including the core electrons.

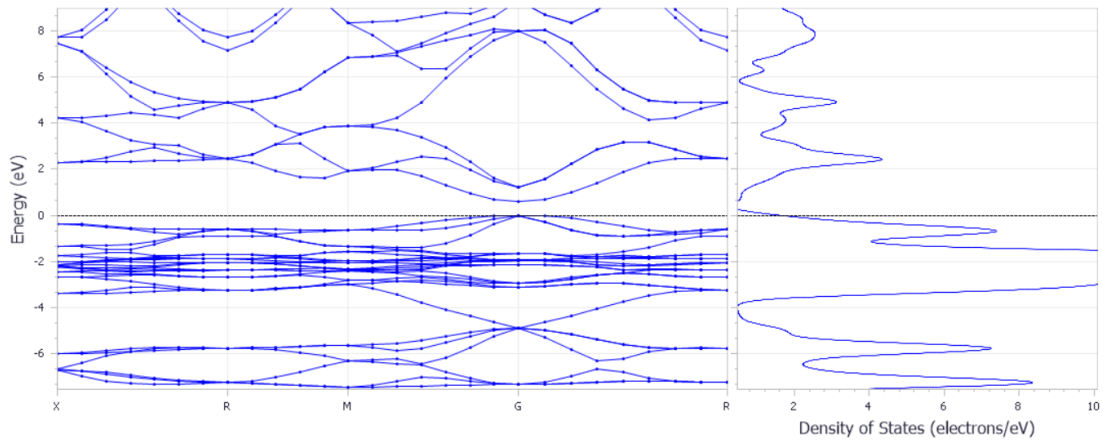


Figure 12(a) Electronic Band Structure and Density of States of Cu_2O calculated with GGA using CASTEP.

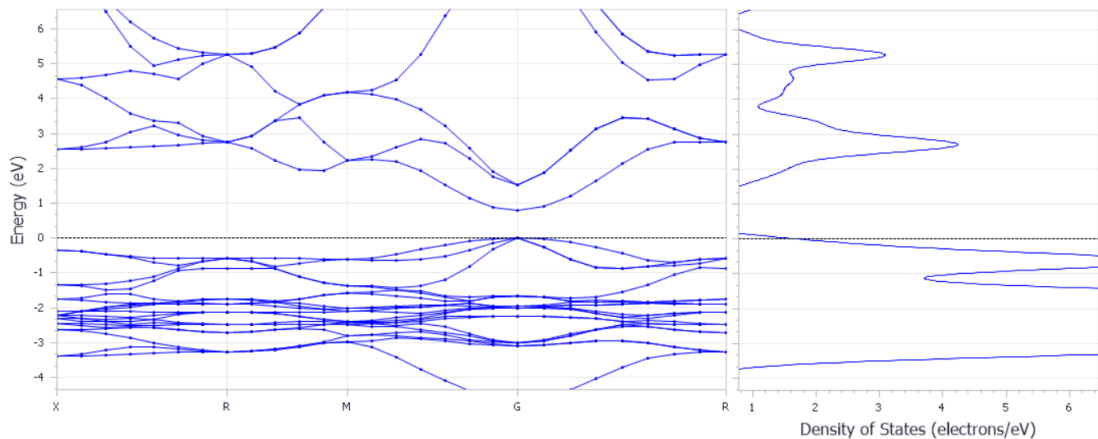


Figure 12(b) Electronic Band Structure and Density of States of Cu_2O calculated with meta-GGA using CASTEP.

The electronic band structure of the system was determined through the utilization of the generalized gradient approximation (GGA) within the framework of density functional theory (DFT). The calculated bandgap value obtained from this GGA-based calculation was found to be 0.59 eV. It is important to note that this value underestimates the experimentally observed bandgap range of 1.8 eV to 2.4 eV [42], which is widely accepted as the true bandgap for the system.

To improve the accuracy of the calculated bandgap, the calculation was repeated using the meta-generalized gradient approximation (m-GGA). This led to a revised bandgap value of 0.8 eV, which is closer to the experimental range.

In order to further reduce the underestimation of the bandgap, it is expected that performing calculations using hybrid functional approximations would yield more accurate results. These hybrid functional approximations incorporate a combination of the exchange-correlation functionals from DFT with a fraction of exact exchange, which has been demonstrated to provide improved bandgap values in comparison to GGA or m-GGA alone [44].

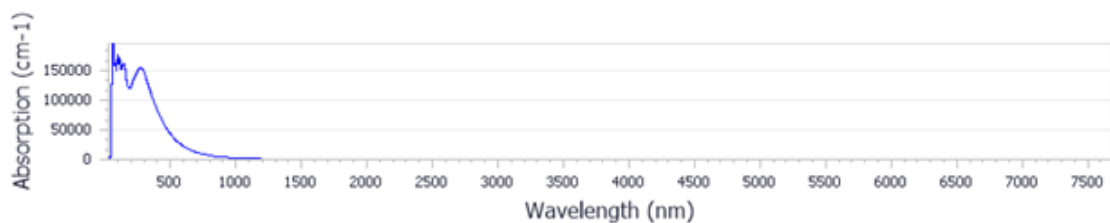


Figure 13 Optical Absorption Spectrum of Cu_2O calculated with GGA using CASTEP.

Copper (I) oxide exhibits favourable absorption characteristics in the UV/visible region, enabling it to effectively absorb photons that pass through the Nickel Oxide hole transport layer, thereby generating photocurrent.

Copper (I) oxide possesses a suitable bandgap energy that allows it to absorb photons in the UV/visible wavelength range. This bandgap energy is smaller than that of Nickel Oxide, resulting in Copper (I) oxide's ability to absorb photons with lower energy. When photons traverse the Nickel Oxide layer, which has low absorption in the UV/visible region, a significant portion of these photons can reach the Copper (I) oxide layer. Upon reaching the Copper (I) oxide layer, the photons with sufficient energy can be absorbed, leading to the generation of electron-hole pairs.

CHARACTERIZATION METHODS

7.1 Contact Angle Measurement

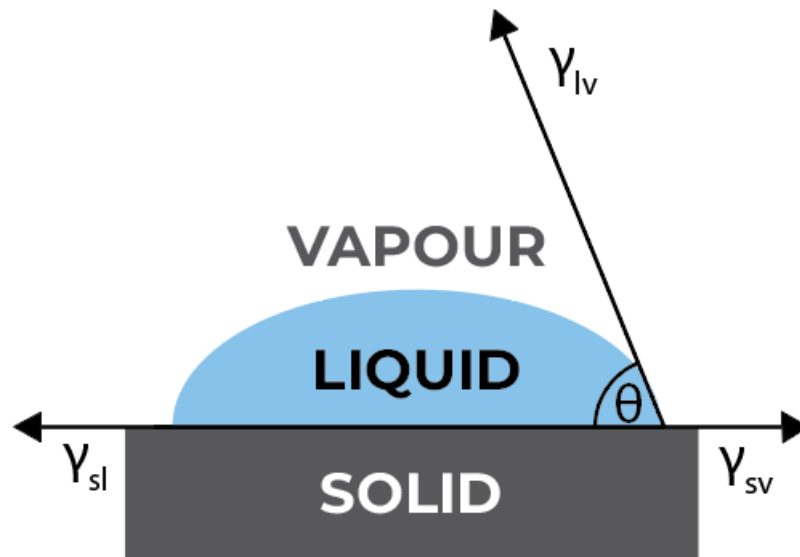


Figure 11 Schematic showing a liquid droplet making a contact angle θ , with the interfacial energies existing in the system.

Contact angle refers to the angle formed at the three-phase boundary between a liquid droplet, the solid surface, and the surrounding gas or liquid phase. It is determined by the balance between intermolecular forces at the interface, including cohesive forces within the liquid and adhesive forces between the liquid and the solid surface [22]. The contact angle provides valuable information about the wetting behaviour of the liquid on the surface, ranging from complete spreading (low contact angle) to non-spreading or droplet formation (high contact angle).

There are several methods for contact angle measurement, including the sessile drop method, captive bubble method, and Wilhelmy plate method [23, 24, 25]. The most commonly used method is the sessile drop method, in which a liquid droplet is placed on the solid surface, and the contact angle is measured from the image of the droplet shape. Advanced techniques such as dynamic contact angle analysis, pendant drop method, and axisymmetric drop shape analysis (ADSA) can provide

additional insights into the dynamic wetting behaviour and contact angle hysteresis.

Contact angle measurement instruments typically consist of a high-resolution camera, a lighting system, and software for image analysis. The camera captures the image of the droplet on the solid surface, while the lighting system provides controlled illumination to enhance droplet visibility. The software enables accurate measurement of the contact angle from the captured images, often incorporating image processing algorithms for edge detection and contact angle calculation.

Contact angle measurement data can be analysed using various approaches, including Young's equation, which relates the contact angle to the interfacial tensions between the liquid, solid, and surrounding medium.

$$\gamma_{sv} = \gamma_{sl} + \gamma_{lv} \cos\theta$$

Statistical analysis can be performed to determine the average contact angle and its variability across multiple measurements. Additionally, contact angle hysteresis, which refers to the difference between advancing and receding contact angles, can provide insights into the surface roughness, heterogeneity, and energy heterogeneity of the solid surface [26].

7.2 Scanning Electron Microscopy

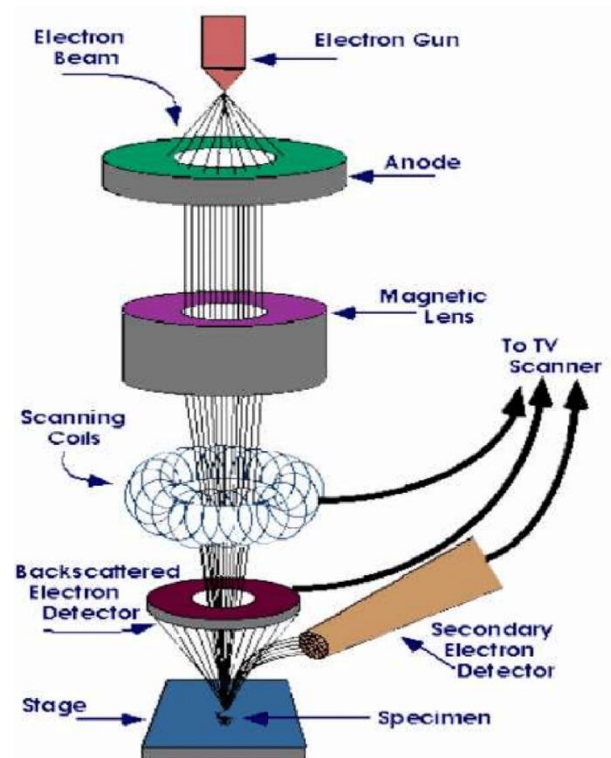


Figure 12 Schematic showing the working principle of the Scanning Electron Microscope [46]

In SEM, a focused beam of high-energy electrons is scanned across the surface of the sample. These electrons are typically generated by an electron gun, which uses a heated filament to emit electrons. The electron beam is then accelerated and focused using electromagnetic lenses [27].

When the electron beam interacts with the sample, several different interactions occur, resulting in the emission of various signals. The three primary signals detected in SEM are secondary electrons (SE), backscattered electrons (BSE), and characteristic X-rays.

Secondary electrons are low-energy electrons that are generated when the primary electron beam strikes the sample surface. These secondary electrons provide information about the topography and surface features of the sample. They are highly sensitive to the local surface properties and are responsible for generating the high-resolution images in SEM [28].

Backscattered electrons, on the other hand, are higher energy electrons that are deflected by the atomic nuclei in the sample. These electrons have energies close

to that of the incident beam and provide information about the sample's composition and atomic number. The intensity of backscattered electrons is influenced by the atomic number and density of the elements present in the sample [29].

In addition to secondary and backscattered electrons, SEM can also detect characteristic X-rays emitted by the sample. When the primary electron beam interacts with the atoms of the sample, it can cause the displacement of inner-shell electrons. As these vacancies are filled by outer-shell electrons, characteristic X-rays are emitted. These X-rays carry elemental information about the sample, allowing for elemental analysis and mapping.

The signals emitted from the sample are collected by detectors placed above or below the sample. For secondary electrons, a scintillator or semiconductor detector is typically used. For backscattered electrons, a solid-state or scintillator detector is employed. For X-ray detection, an energy-dispersive X-ray spectrometer (EDS) or wavelength-dispersive X-ray spectrometer (WDS) is used [30].

A typical SEM consists of four essential components: an electron source, electron lenses, a sample stage, and detectors. The electron source, usually a heated tungsten filament or a field emission gun, generates a beam of electrons. Electron lenses focus and scan the beam across the sample's surface. The sample stage holds the specimen and provides precise control over its position. Detectors collect and analyze the signals emitted from the sample, producing images and other analytical data.

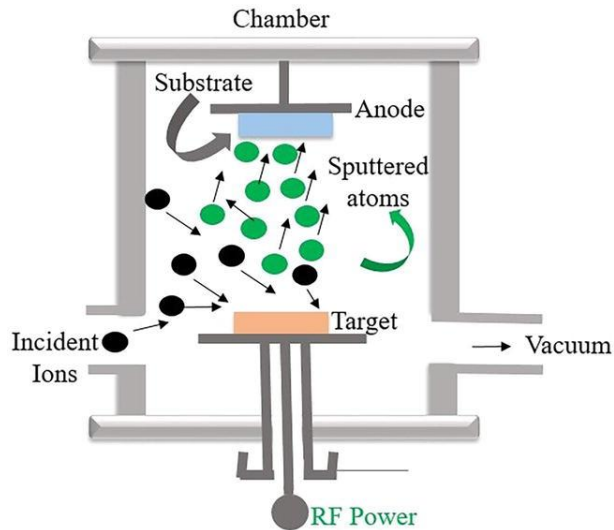


Figure 13 Schematic showing the sputtering process required for the preparation non-conductive samples. [47]

To obtain high-quality SEM images, proper sample preparation is crucial. The sample should be carefully chosen and prepared to meet specific research objectives. Generally, samples need to be conductive or made conductive through techniques like sputter coating with a thin layer of conductive material, such as gold or carbon. This ensures proper charge dissipation and minimizes image distortions caused by charging effects.

7.3 Energy Dispersive X-Ray Spectroscopy

Energy Dispersive X-ray Spectroscopy (EDS or EDX) is a technique used to analyze the elemental composition of a sample. It is commonly coupled with scanning electron microscopy (SEM) to provide detailed information about the chemical elements present in the sample.

When a sample is bombarded with a high-energy electron beam in an SEM, the electrons interact with the atoms in the sample. These interactions can cause the displacement of inner-shell electrons, creating vacancies in the electron shells. As these vacancies are filled by outer-shell electrons, energy is released in the form of X-rays. These X-rays have specific energies corresponding to the differences in energy levels between the electron shells [31].

The characteristic X-rays emitted by the sample contain information about the elements present in the sample and their relative abundances. Each element has a unique set of energy levels and, therefore, emits characteristic X-rays at specific

energies. By detecting and analyzing these X-rays, it is possible to identify the elements present in the sample.

The detection of characteristic X-rays in EDS is accomplished using a solid-state detector; typically a silicon drift detector (SDD). When X-rays interact with the detector, they generate electron-hole pairs, which create a measurable electrical signal. The energy of the X-rays is directly related to the voltage generated by the detector.

7.4 Optical Profilometry

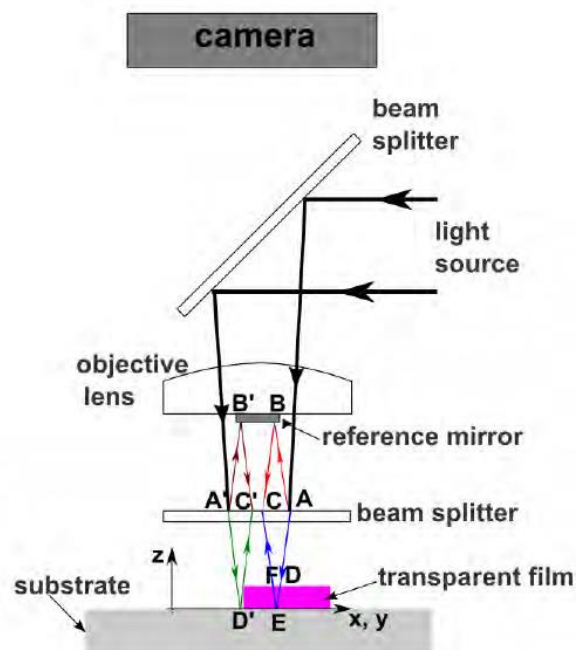


Figure 14 Schematic showing the working principle of the setup used for Optical Profilometry. [48]

Optical profilometry is a non-contact measurement technique used to obtain precise three-dimensional surface topography information of an object. It utilizes the principles of optics and interferometry to determine the height variations on a surface. The physics behind optical profilometry involves the interference of light waves and the analysis of the resulting interference patterns.

In optical profilometry, a beam of light, usually from a laser source, is directed towards the sample surface. The light beam is then reflected or scattered back from the surface, and the reflected light is collected by a detector, such as a camera

or a photodiode array. The reflected light carries information about the surface topography.

The basic principle behind optical profilometry is based on the interference of the reflected light waves. When the light waves from the sample surface are combined with a reference wave, interference occurs. This interference pattern carries information about the height variations of the surface [32].

There are different methods of optical profilometry, but one commonly used technique is called white-light interferometry. In this technique, a white-light source is used instead of a laser. The white light is split into two beams: a reference beam and a measurement beam. The reference beam is directed towards a reference mirror, while the measurement beam is directed towards the sample surface.

The measurement beam is reflected from the surface, and the reflected light interferes with the reference beam. The interference pattern is then captured by the detector. The interference pattern changes as the distance between the reference mirror and the surface varies, resulting in different phases of the light waves at different points on the surface. By analysing the interference pattern, the height variations of the surface can be calculated. The primary components of an optical profilometer include a light source, an objective lens, a detector, and a scanning or stage system. The light source emits coherent or structured light, such as laser light or fringe patterns, onto the sample's surface. The objective lens collects the reflected light and focuses it onto the detector, which captures the interference patterns. The scanning or stage system allows for precise movement of the sample, enabling the acquisition of multiple measurements across the surface.

Optical profilometry employs various measurement techniques, including white light interferometry, confocal microscopy, and phase-shifting interferometry [33, 34, 35]. White light interferometry uses broadband light sources and spectrally separates the reflected light to create interference patterns. Confocal microscopy uses a small aperture to eliminate out-of-focus light, resulting in improved axial resolution. Phase-shifting interferometry involves systematically shifting the phase of the incident light to obtain multiple interferograms, which are then combined to reconstruct the surface profile.

7.5 UV/Vis Spectroscopy

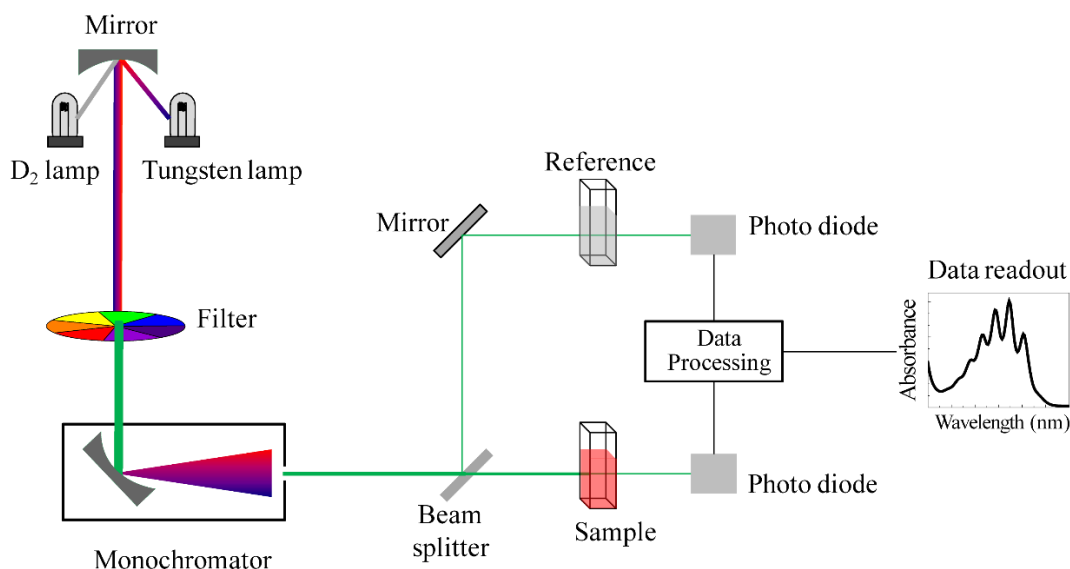


Figure 158 Schematic showing the working principle of a UV/Vis Spectrophotometer.

When a molecule is irradiated with UV or Vis light, the photons can be absorbed if their energy matches the energy difference between two electronic states of the molecule. The electronic states include the ground state, which represents the lowest energy level of the molecule, and excited states, which correspond to higher energy levels. These transitions occur due to the excitation of electrons within the molecule [36].

The energy of a photon is inversely proportional to its wavelength, according to the equation:

$$E = \frac{hc}{\lambda}$$

where E is the energy, h is Planck's constant, c is the speed of light, and λ is the wavelength of light. Therefore, UV light, which has a shorter wavelength and higher energy, can cause transitions to higher energy electronic states compared to visible light [37].

The absorption of UV or Vis light by a molecule is related to its electronic structure and the availability of energy levels for electronic transitions. Each molecule has a unique set of energy levels determined by its molecular orbital configuration. In

UV/Vis spectroscopy, the electronic transitions involved are typically those between the highest occupied molecular orbital (HOMO) and the lowest unoccupied molecular orbital (LUMO).

The energy of these electronic transitions determines the wavelength or energy of light that will be absorbed. The absorption spectrum of a molecule or material is obtained by measuring the intensity of light transmitted through a sample as a function of the wavelength or energy of the incident light. The spectrum shows the wavelengths or energies at which the sample absorbs light, resulting in a decrease in the transmitted intensity [38].

The intensity of absorption is related to the concentration of the absorbing species, the path length of the light through the sample, and the molar absorptivity or extinction coefficient of the substance. The molar absorptivity represents the efficiency with which a compound absorbs light at a given wavelength.

A typical UV/Vis spectrophotometer consists of a light source, a monochromator, a sample holder, a detector, and a data acquisition system. The light source emits a broad range of UV/Vis wavelengths. The monochromator selects a specific wavelength of light for analysis. The sample holder accommodates the sample, which is typically in liquid or solid form. The detector measures the intensity of light transmitted through or absorbed by the sample. The data acquisition system records the intensity values and generates a UV/Vis spectrum.

UV/Vis spectra provide quantitative and qualitative information about the sample. The absorption spectrum is obtained by plotting the absorbance (or transmittance) versus wavelength. The spectra can be analyzed to determine the position and intensity of absorption peaks, which correspond to electronic transitions. Quantitative analysis can be performed using Beer-Lambert's law, which relates the absorbance to the concentration of the absorbing species. Data analysis software allows for peak identification, spectral comparison, and calculation of molar absorptivity and concentration.

7.6 RAMAN Spectroscopy

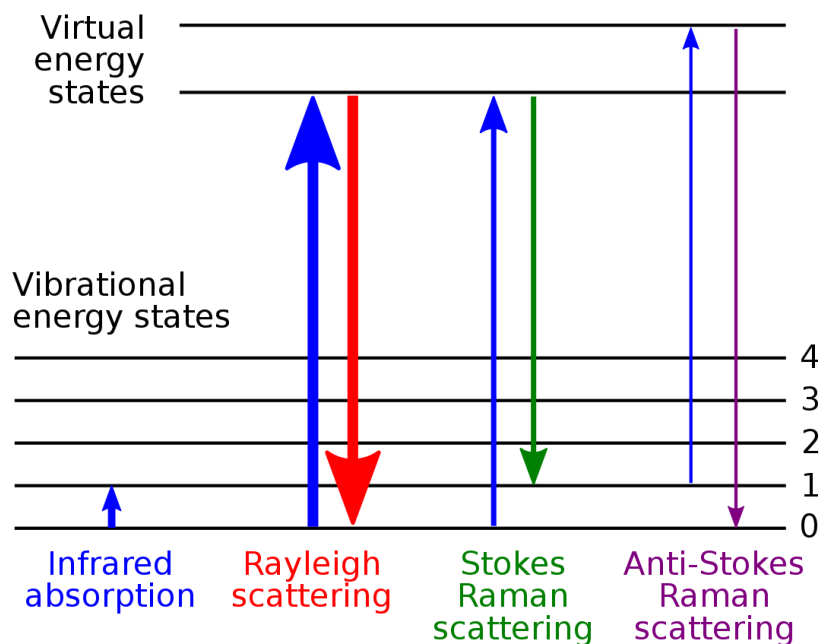


Figure 169 Schematic representation of the scattering modes in RAMAN Spectroscopy.

When a sample is irradiated with monochromatic light, most of the incident photons undergo elastic scattering, known as Rayleigh scattering. However, a small fraction of the photons experience inelastic scattering, known as Raman scattering [39].

The Raman effect arises from the interaction of photons with the vibrational and rotational energy levels of molecules. When a photon interacts with a molecule, it can transfer energy to the molecule, causing it to undergo a transition from the ground state to a higher energy vibrational or rotational state. This process is known as Stokes scattering. Alternatively, the molecule can lose energy and transition to a lower energy state, resulting in anti-Stokes scattering.

The energy difference between the incident and scattered photons corresponds to the energy of the molecular vibration or rotation. This energy difference is known as the Raman shift. The Raman shift can be measured as the difference in wavelength between the incident and scattered light, which can be detected using a spectrometer.

Raman spectroscopy can provide valuable information about molecular structure, including bond lengths, bond angles, and the presence of functional groups. Each molecular species has a unique Raman spectrum, allowing for identification and characterization of chemical compounds.

A typical Raman spectrometer consists of a laser light source, a monochromator or filter, a sample holder, a detector, and a data acquisition system. The laser light source emits a monochromatic beam of light, typically in the visible or near-infrared range. The monochromator or filter selects the desired wavelength of the Raman-shifted light for analysis. The sample holder holds the sample under investigation, which can be in the form of solids, liquids, or gases. The detector measures the intensity of the Raman-scattered light, and the data acquisition system records the spectral information [40].

Raman spectra are typically presented as plots of intensity versus Raman shift, which represents the energy difference between the incident and scattered light. Data analysis involves the identification and interpretation of spectral peaks, which correspond to specific molecular vibrations. Raman spectra can be compared to reference spectra or analyzed using spectral databases to identify unknown substances. Quantitative analysis can be performed by correlating Raman intensity with sample concentration or by utilizing calibration curves.

RESULTS AND DISCUSSION

8.1 Effect of UV/Ozone Treatment on the surface wettability of substrate

Table 1 Results from Contact Angle measurement.

#	Time (min)	Contact Angle (degree)	
		Plane glass	FTO glass
1	0	43.25	47.35
2	5	30.8	16.8
3	10	20.2	11
4	15	14.45	--
5	30	--	9.4
6	45	11.85	0

The present study aimed to investigate the effects of UV/Ozone Treatment on the surface wettability of FTO glass and Plane glass substrates. The evaluation of surface wettability was carried out using a sessile water droplet and a high-resolution camera, coupled with a goniometer to accurately measure the contact angle formed at the Solid-Liquid interface.

The obtained results clearly demonstrate a significant decrease in the contact angle, indicating an enhanced wettability of the surfaces upon increased exposure to the UV/Ozone environment. This observation can be attributed to the removal of organic impurities present on the surface, which undergo chemical interactions with ozone. As a result of this chemical interaction, volatile compounds are formed

and subsequently removed from the experimental chamber [41]. The removal of these contaminants yields a surface that is free from impurities and possesses a higher surface energy, thereby facilitating improved adhesion of thin films.

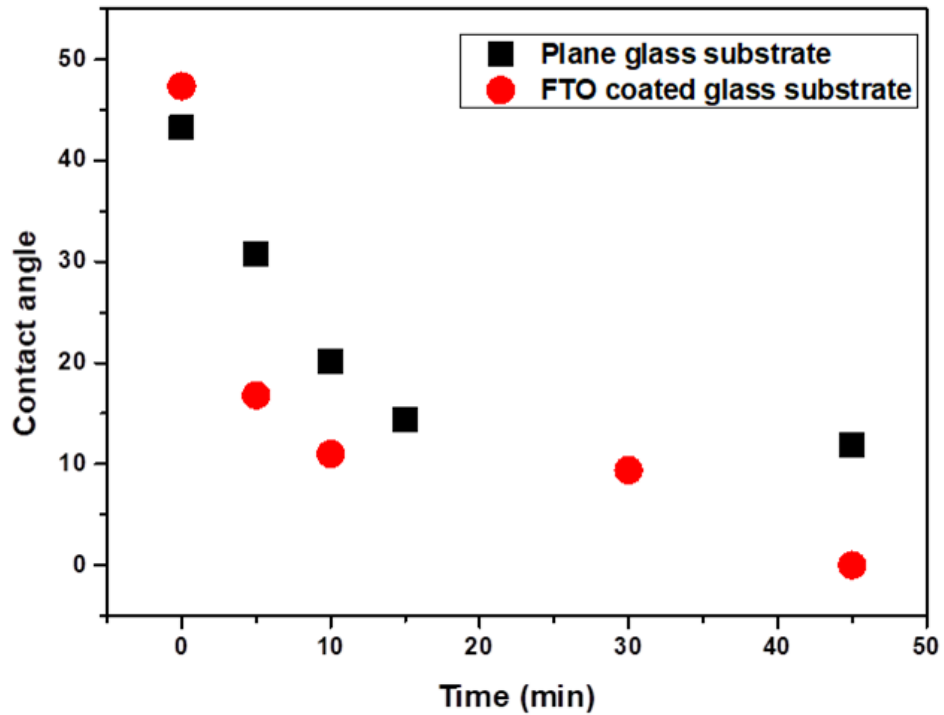


Figure 20 Plot of Contact Angle against time under UV/Ozone Treatment

The improved wettability observed in FTO glass after the removal of contaminants can be attributed to several factors. Firstly, FTO coatings typically exhibit a rougher surface compared to plain glass. This increased surface roughness results in a larger effective surface area, leading to a greater number of exposed atoms or molecules at the surface. Consequently, the higher surface area contributes to an overall higher surface energy.

Moreover, FTO coatings are doped with fluorine atoms, which introduce additional polar groups onto the surface. These polar groups have the ability to interact with other polar molecules, such as water, through dipole-dipole interactions. These interactions contribute to an elevated surface energy in comparison to the non-doped glass surface.

The combination of increased surface roughness and the presence of polar groups on the FTO surface contribute to the enhanced wettability observed. The removal of contaminants through UV/Ozone Treatment further improves the cleanliness of the surface, allowing for better adhesion and interaction with the sessile water droplet.

8.2 Analysis of Morphological Characteristics of the hole

transport layer

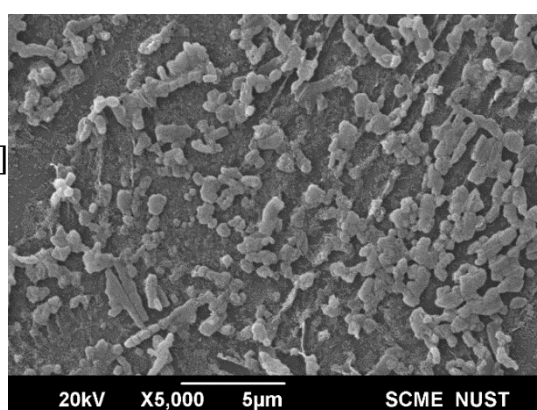


Figure 21(a) Surface Morphology of NiO coated on plain glass slide with a dwell time of 0 minutes.

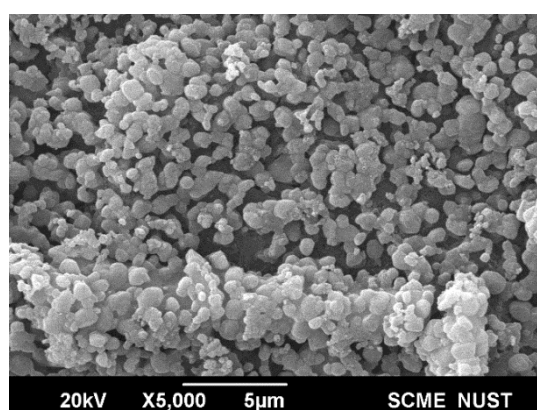


Figure 21(b) Surface Morphology of NiO coated on Plain glass slide with a dwell time of 5 minutes.

The surface morphology of the Nickel Oxide (NiO) layer employed as the hole transport layer was investigated using Scanning Electron Microscopy (SEM) to assess the surface coverage on both Plain glass and FTO glass substrates. A comparative analysis was conducted between films dip coated with a 0-minute dwell time and those with a 5-minute dwell time. It is crucial for the hole transport layer to exhibit a surface free from micro or nano-scale pinholes to prevent shunting.

The SEM images of the films on the plain glass substrate indicate a substantial influence of the dwell time on the surface coverage. Specifically, the film with a 0-minute dwell time displays significantly less coverage in comparison to the film with a 5-minute dwell time. However, it should be noted that the observed morphology is porous and composed of nanoparticles as building blocks. This porous nature of the film facilitates the infiltration of the solution-processable

Cu₂O layer through the NiO film, promoting direct contact between the transparent conductive oxide (TCO) and the photoactive layer.

Unfortunately, the formation of such shunting paths is a potential consequence of this infiltration. Shunting occurs when there is an unintended electrical connection or short circuit between the TCO and the photoactive layer, which can degrade the performance of the device.

Therefore, while the increased dwell time improves the surface coverage of the NiO layer, the porous morphology and nanoparticle-based structure still allow for the infiltration of the solution-processable Cu₂O layer. This infiltration can lead to shunting, compromising the device's efficiency.

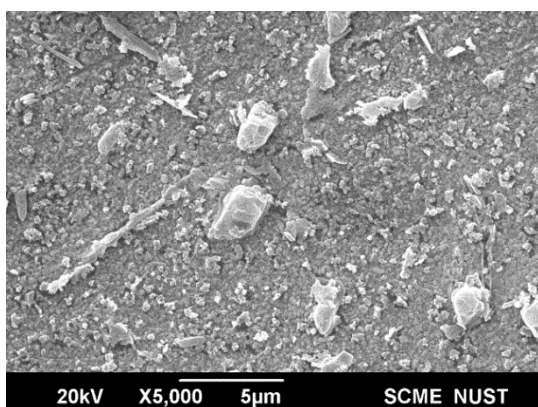


Figure 22(a) Surface Morphology of NiO coated on FTO substrate with a dwell time of 0 minutes.

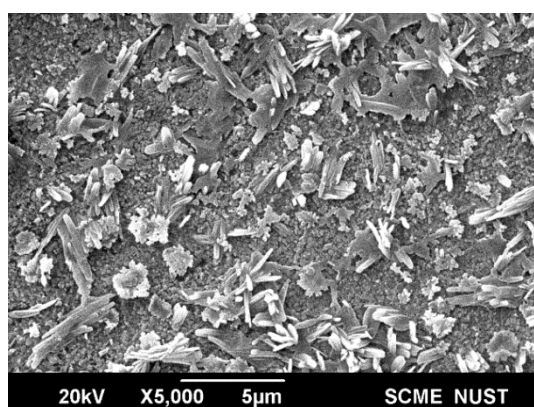


Figure 22(b) Surface Morphology of NiO coated on FTO substrate with a dwell time of 5 minutes.

The films coated on an FTO glass substrate on the other hand show much better morphological characteristics. Complete surface coverage is seen to be achieved; this may be attributed to the texture of the substrate surface which provides a larger number of nucleation sites close to each other.

8.3 Elemental Analysis of the hole transport layer

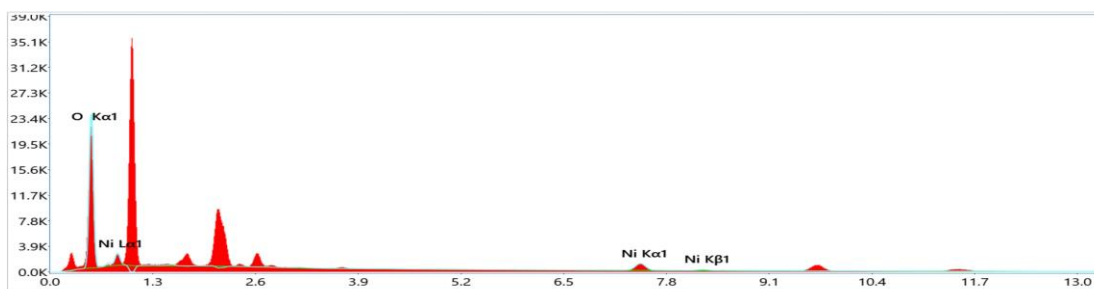


Figure 23(a) EDX Results for NiO coated on plain glass slide with a dwell time of 0 minutes.

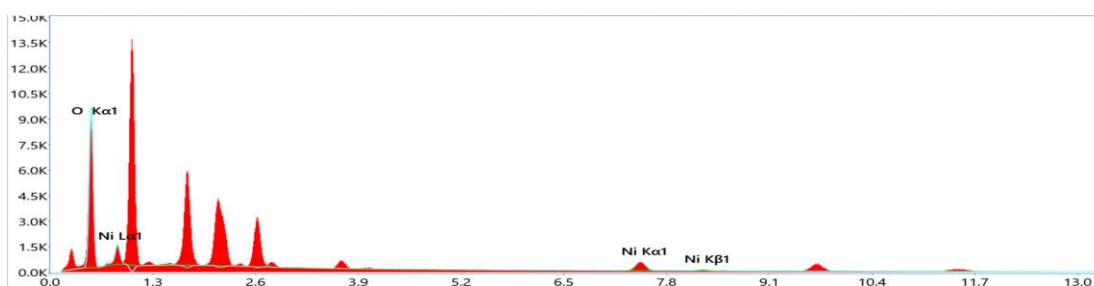


Figure 23(b) EDX Results for NiO coated on plain glass slide with a dwell time of 5 minutes.

Table 2 Atomic and Weight percentages of the elements obtained from EDX Analysis.

Dwell time	Element	Weight %	Atomic %
0 min	O	78.7	93.1
	Ni	21.3	6.9
5 min	O	75.2	91.8
	Ni	24.8	8.2

Energy Dispersive X-Ray Spectroscopy (EDS) analysis was conducted to examine the composition of the deposited NiO thin films on a plane glass substrate. The obtained results confirm the formation of the Nickel Oxide thin film; however, the atomic and weight percentages deviate from the anticipated ranges based on the given stoichiometric ratios. This discrepancy can be attributed to the phenomenon of X-ray penetration through the thin film, as well as the higher atomic and weight percentage of oxygen arising from the presence of oxides in the substrate.

During the EDS analysis, X-rays are emitted and interact with the sample, causing characteristic X-rays to be generated. The detection of these X-rays provides information about the elemental composition of the sample. However, in the case of thin films, X-rays can penetrate through the film, resulting in signal contributions from both the film and the underlying substrate.

Consequently, the observed atomic and weight percentages may not accurately reflect the true composition of the NiO thin film alone, as the signal detected includes contributions from the substrate. In this context, the higher atomic and weight percentage of oxygen can be attributed to the presence of oxides within the substrate material.

8.4 Characterization of film thickness for the hole transport layer

layer

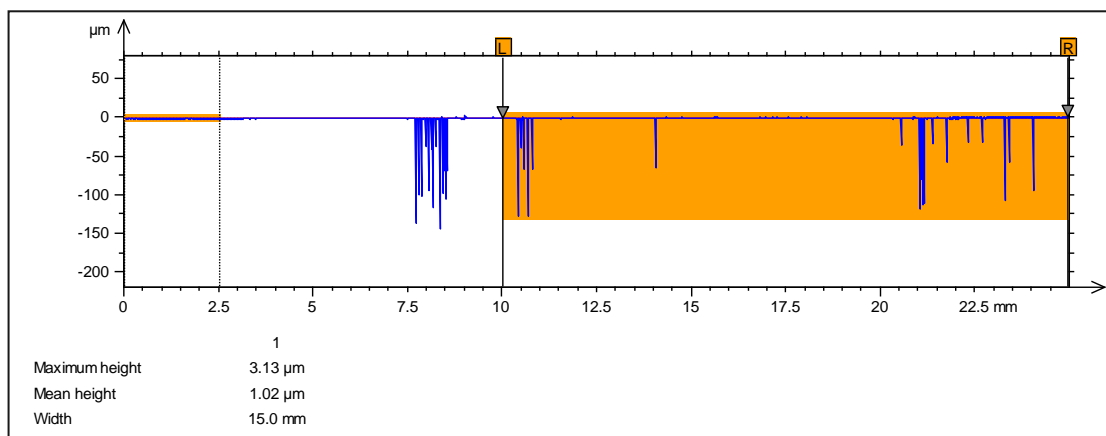


Figure 2417(a) Optical Profilometry results for NiO film deposited on plain glass substrate with a dwell time of 0 minutes.

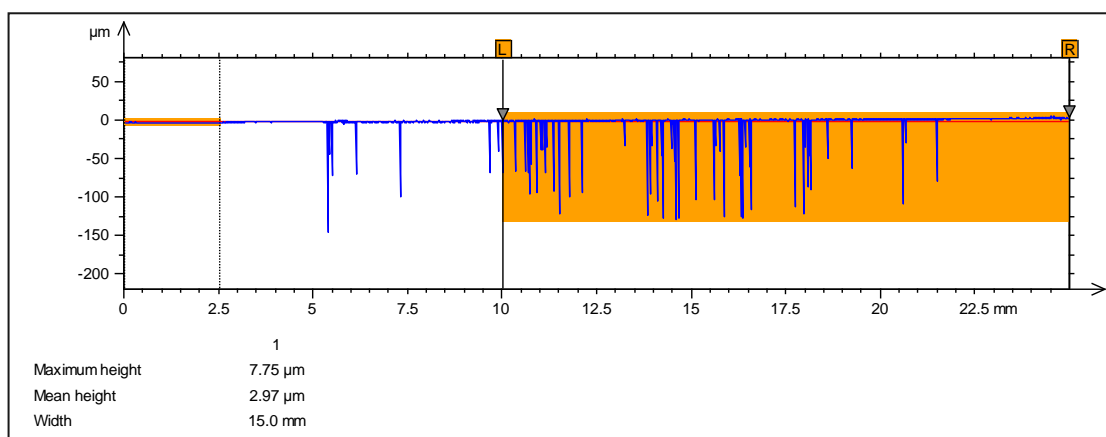


Figure 24(b) Optical Profilometry results for NiO film deposited on plain glass substrate with a dwell time of 5 minutes.

To confirm the roughness and thickness of the film, optical profilometry was employed on the NiO coated on plane glass substrate. This technique is widely used to measure the topography of a surface with high precision and accuracy.

Table 3 Mean Thickness and Mean Roughness of film resulting from variation in dip coating dwell time.

Dwell time	Mean thickness (μm)	Mean roughness (μm)	Max height (μm)
0 min	1.02	0.329	3.13
5 min	2.97	1.01	7.75

As depicted in the table above, there is a significant increase in the film thickness and surface roughness with an increase in the dwell time.

8.5 Investigation of the optical properties of the photoactive layer

layer

The optical properties of the Cu_2O photoactive layer were examined through the use of UV/Vis Spectroscopy. The films deposited with SILAR cycles of 20, 40 and 60 were tested under incident electromagnetic radiations of 300 nm to 900 nm.

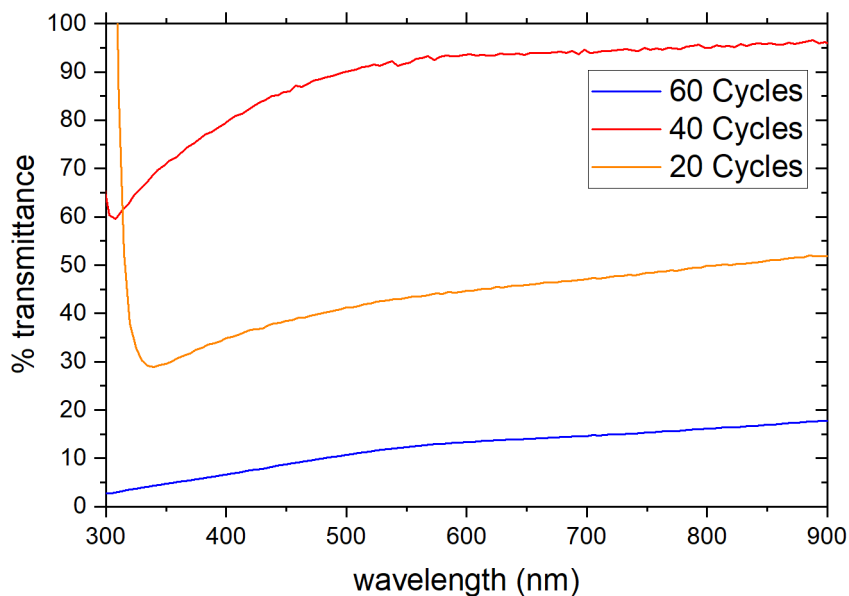


Figure 25(a) Percentage Transmission of Cu_2O films as a function of incident wavelength deposited on plain glass substrate with 20, 40 and 60 SILAR cycles.

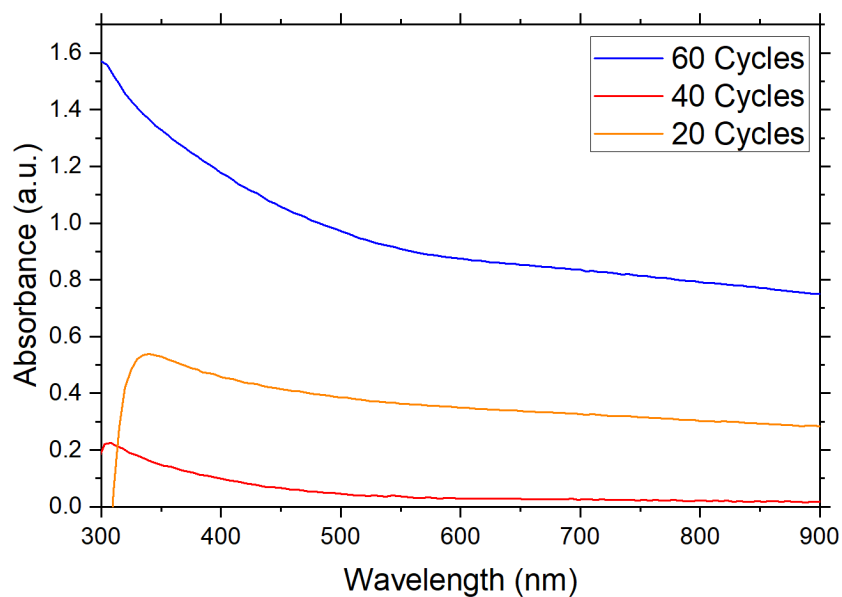


Figure 25(b) Optical Absorption Spectra for Cu_2O films deposited on plain glass substrate with 20, 40 and 60 SILAR cycles.

The optical absorption spectra analysis reveals that the highest absorbance of the film is obtained with 60 Successive Ionic Layer Adsorption and Reaction (SILAR) cycles. However, the anticipated trend is an increase in absorbance with respect to the number of SILAR cycles. Nevertheless, the observed anomaly in the film with 20 cycles can be attributed to the contamination of the methanol rinsing medium with Cu_2O , leading to a greater than expected film thickness. It is proposed that the contamination of the methanol rinsing medium occurred during the SILAR process, resulting in the incorporation of Cu_2O into the film. This contamination, in turn, affected the film thickness and subsequently influenced the optical absorption spectra. To mitigate such issues, it is recommended to replace the rinsing medium at regular intervals between SILAR cycles. By ensuring the cleanliness of the rinsing medium, the chances of contamination and deviations from the expected absorbance trend can be minimized.

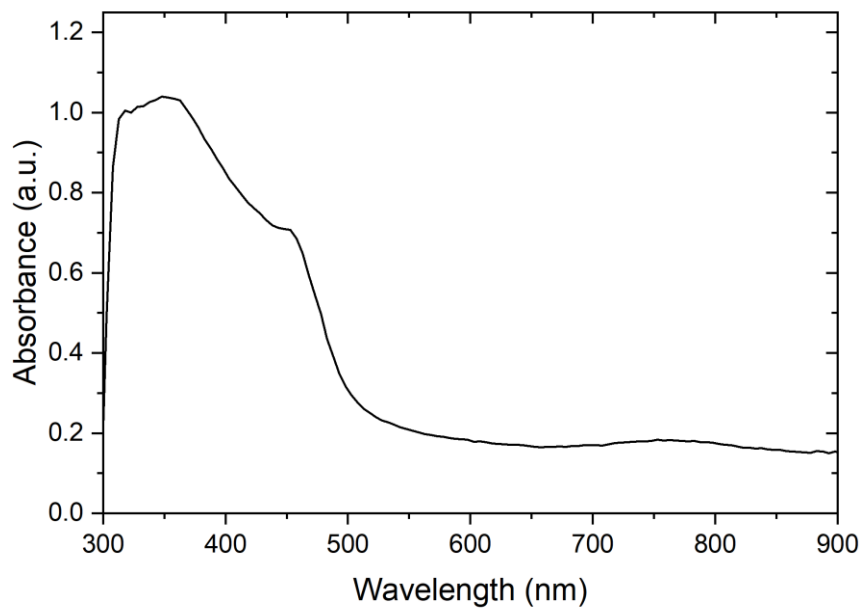


Figure 26 Optical Absorption Spectrum for Cu_2O deposited on FTO glass substrate through electrodeposition.

Cu_2O film deposited on FTO substrate through electrodeposition shows a trend similar to that shown by films deposited on glass substrate by SILAR method.

8.6 Compositional Analysis of the photoactive layer

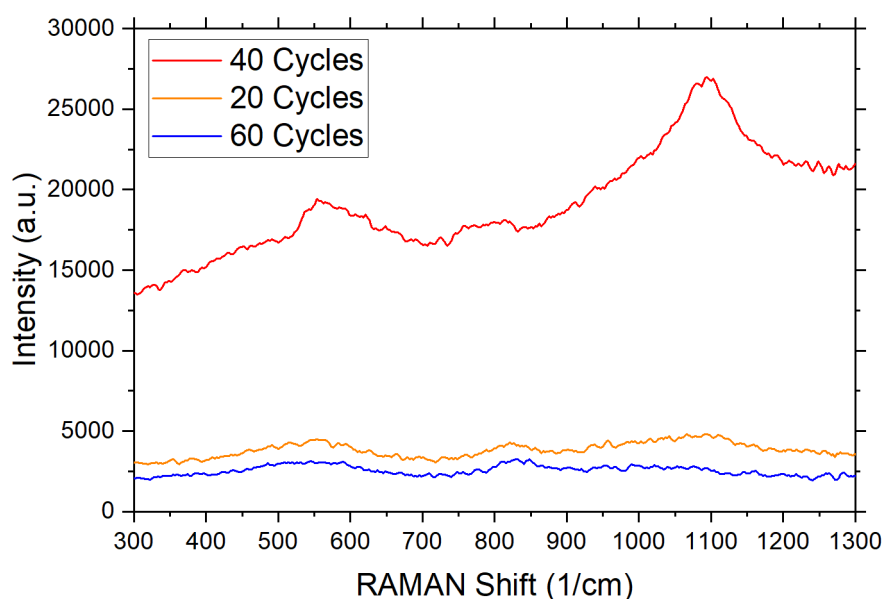


Figure 27 RAMAN Spectroscopy results for Cu_2O films deposited on plain glass substrate with 20, 40 and 60 SILAR cycles.

The composition analysis of the thin films was carried out using RAMAN Spectroscopy, which revealed peaks at 550 cm^{-1} and 1050 cm^{-1} . These peak positions correspond well with the results obtained by Mohamed Shaban et al. [45], providing confirmation of the successful attainment of the desired composition in the thin films.

Furthermore, it was observed that the intensity of the RAMAN peaks is inversely related to the thickness of the film. As a general trend, thinner films tend to exhibit higher intensity signals in RAMAN Spectroscopy. However, the anomalous reading obtained for the film deposited with 20 SILAR cycles can once again be attributed to the contamination of the methanol rinsing medium, leading to the deposition of a thicker film than anticipated.

The contamination of the rinsing medium with unwanted materials, such as Cu_2O , can impact the film thickness and subsequently affect the RAMAN peak intensities. In this case, the presence of a thicker film resulted in a deviation from the expected intensity trend.

Therefore, in order to obtain reliable and consistent results in future experiments, it is crucial to ensure the cleanliness of the rinsing medium and prevent any

potential contamination. By taking measures to avoid contamination, such as replacing the rinsing medium at regular intervals between SILAR cycles, more accurate and representative RAMAN spectra can be obtained, aiding in the precise characterization of thin film composition.

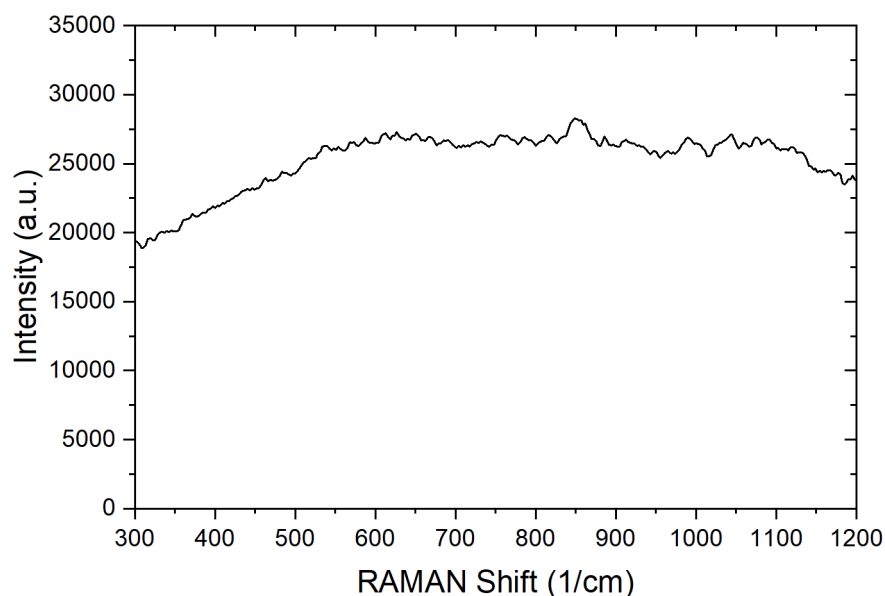


Figure 28 RAMAN Spectroscopy results for Cu₂O deposited on FTO glass substrate through electrodeposition.

The RAMAN spectra acquired for Cu₂O deposited on an FTO substrate through electrodeposition exhibit the absence of resolvable peaks. This outcome is most likely attributed to the interference of the FTO substrate's peaks with the peaks originating from the Cu₂O film. As a consequence, the overall pattern appears noisy and lacks discernible features. Consequently, it is not possible to draw any conclusive findings from this result.

CONCLUSION

Although the efficiency of Cu₂O is limited by the Shockley-Queisser limit due to a relatively large bandgap, its practical implementation remains viable. Especially, when a large number of metal oxide based photovoltaic devices may be used together; as in Building Integrated Photovoltaics (BIPVs). The semitransparent appearance of metal oxides make them an attractive option for energy generation in applications like solar windows. Likewise, the experimentation has shown that the number of SILAR cycles impacts the film quality significantly. Further investigation will be required to accurately determine the effects of deposition methods and parameters on the film morphology. In addition, the application of density functional theory (DFT) simulations facilitates the selection of suitable materials by enabling a simulated comparison of optoelectronic properties. However, it is important to acknowledge that calculations yielding properties closer to experimental values require higher computing power, necessitating a compromise in computational resources.

REFERENCES

- 1] IEA., O. E. C. D. "World energy investment 2017." Paris, France: IEA, 2017.
- 2] Ashok, S.. "solar energy." Encyclopedia Britannica, June 6, 2023.
- 3] Solar spectrum: Solar radiation and irradiance Ossila.
- 4] U.S. Energy Information Administration - EIA - independent statistics and analysis Photovoltaics and electricity - U.S. Energy Information Administration (EIA).
- 5] Masood, M.T. (1970) Solution-processable compact and mesoporous titanium dioxide thin films as electron-selective layers for perovskite solar cells, Solution-Processable Compact and Mesoporous Titanium Dioxide Thin Films as Electron-Selective Layers for Perovskite Solar Cells | Åbo Akademis bibliotek | Finna.fi.
- 6] Pastuszak, J. and Węgierek, P. (2022) Photovoltaic cell generations and current research directions for their development, Materials (Basel, Switzerland).
- 7] F. Zhang, X. Wen, L. Liu, Z. Yuan, and X. Sun, "Recent Progress in Metal Oxide-based Solar Cells: Material and Device Design," Journal of Materials Chemistry A, Mar. 2020.
- 8] 'A review of metal oxide thin films in solar cell applications' (2022) International Journal of Thin Film Science and Technology.
- 9] Rühle S;Anderson AY;Barad HN;Kupfer B;Bouhadana Y;Rosh-Hodesh E;Zaban A; All-oxide photovoltaics, The journal of physical chemistry letters.
- 10] Surface wettability of silica films modified by UV/Ozone Treatment.
- 11] Siddique, M.N. et al. (2018) Investigation of optical properties of nickel oxide nanostructures using photoluminescence and diffuse reflectance spectroscopy, AIP Publishing.
- 12] (No date a) Sci-hub | Determination of the optical band gap for amorphous and nanocrystalline copper oxide thin films prepared by SILAR technique.
- 13] Chatterjee et al. (2015) Formation of all-oxide solar cells in atmospheric condition based on CU₂O thin films grown through Silar Technique, Solar Energy Materials and Solar Cells.
- 14] Determination of the optical band gap for amorphous and nano-crystalline copper oxide thin films prepared by SILAR technique.

- 15] M. T. Taschuk and L. J. Vogel, "Simplifying microstructured polymer film production through optimized glass substrate cleaning," *Langmuir*, Nov. 2011.
- 16] G. Zhao, H. Li, X. Li, Y. Zhang, and X. Wu, "UV/Ozone Surface Modification: A Review," *Journal of Materials Science & Technology*, Apr. 2016.
- 17] R. Nouli "Oxide Coatings for High-Efficiency Multijunction Solar Cells". *IEEE Journal of Photovoltaics*, 2017.
- 18] L. Can "Advances oxide-based materials and devices for photovoltaics" *Nature Reviews Materials*, 2016.
- 19] Kaur, I., & Singh, G. (2019). Dip Coating: A Versatile Technique for Coatings and Thin Films Fabrication. *Surface Engineering and Applied Electrochemistry*.
- 20] Harrison, N. M. (2003). An introduction to density functional theory. *Nato Science Series Sub Series III Computer and Systems Sciences*, 187, 45-70.
- 21] CASTEP GUIDE, MATERIALS STUDIO 2020
- 22] Adam, N. K. (1957). Use of the Term 'Young's Equation' for Contact Angles. *Nature*, 180(4590), 809–810.
- 23] Della Volpe, C., Maniglio, D., Siboni, S., & Morra, M. (2001). An experimental procedure to obtain the equilibrium contact angle from the Wilhelmy method. *Oil & gas science and technology*, 56(1), 9-22.
- 24] Zhang, W., & Hallström, B. (1990). Membrane characterization using the contact angle technique I. Methodology of the captive bubble technique. *Desalination*, 79(1), 1-12.
- 25] Kung, C. H., Sow, P. K., Zahiri, B., & Mérida, W. (2019). Assessment and interpretation of surface wettability based on sessile droplet contact angle measurement: challenges and opportunities. *Advanced Materials Interfaces*, 6(18), 1900839.
- 26] Gao, L., & McCarthy, T. J. (2006). Contact angle hysteresis explained. *Langmuir*, 22(14), 6234-6237.
- 27] Vernon-Parry, K. D. (2000). Scanning electron microscopy: an introduction. *III-Vs Review*, 13(4), 40-44.
- 28] Seiler, H. (1983). Secondary electron emission in the scanning electron microscope. *Journal of Applied Physics*, 54(11), R1-R18.

- 29] Krinsley, D. H., Pye, K., Boggs Jr, S., & Tovey, N. K. (1998). Backscattered scanning electron microscopy and image analysis of sediments and sedimentary rocks (p. 203).
- 30] Shindo, D., Oikawa, T., Shindo, D., & Oikawa, T. (2002). Energy dispersive x-ray spectroscopy. *Analytical electron microscopy for materials science*, 81-102.
- 31] Ngo, P. D. (1999). Energy dispersive spectroscopy. *Failure analysis of integrated circuits: Tools and techniques*, 205-215.
- 32] Ekici, Ömer, et al. "Evaluation of surface roughness after root resection: An optical profilometer study." *Microscopy Research and Technique* 84.4 (2021): 828-836.
- 33] Wyant, J. C. (2002, July). White light interferometry. In *Holography: a tribute to yuri denisyuk and emmett leith* (Vol. 4737, pp. 98-107). SPIE.
- 34] Nwaneshiudu, A., Kuschal, C., Sakamoto, F. H., Anderson, R. R., Schwarzenberger, K., & Young, R. C. (2012). Introduction to confocal microscopy. *Journal of Investigative Dermatology*, 132(12), 1-5.
- 35] Lai, G., & Yatagai, T. (1991). Generalized phase-shifting interferometry. *JOSA A*, 8(5), 822-827.
- 36] Picollo, M., Aceto, M., & Vitorino, T. (2018). UV-Vis spectroscopy. *Physical sciences reviews*, 4(4), 20180008.
- 37] Förster, H. (2004). UV/vis spectroscopy. *Characterization I: -/-*, 337-426.
- 38] Chen, Z., Dinh, H. N., Miller, E., Chen, Z., Deutsch, T. G., Dinh, H. N., ... & Turner, J. (2013). UV-vis Spectroscopy. *Photoelectrochemical Water Splitting: Standards, Experimental Methods, and Protocols*, 49-62.
- 39] Long, D. A. (1977). *Raman spectroscopy. New York, 1*.
- 40] Lyon, L. A., Keating, C. D., Fox, A. P., Baker, B. E., He, L., Nicewarner, S. R., ... & Natan, M. J. (1998). Raman spectroscopy. *Analytical Chemistry*, 70(12), 341-362.
- 41] Vig, J. R. (1985). UV/ozone cleaning of surfaces. *Journal of Vacuum Science & Technology A: Vacuum, Surfaces, and Films*, 3(3), 1027-1034.
- 42] Oudah, M. H., Hasan, M. H., & Abd, A. N. (2020, March). Synthesis of copper oxide thin films by electrolysis method based on Porous Silicon for Solar Cell Applications.
- 43] Shi, M., Qiu, T., Tang, B., Zhang, G., Yao, R., Xu, W., ... & Peng, J. (2021). Temperature-controlled crystal size of wide band gap nickel oxide and its application in electrochromism. *Micromachines*, 12(1), 80.

- 44] Simón, L., & Goodman, J. M. (2011). How reliable are DFT transition structures? Comparison of GGA, hybrid-meta-GGA and meta-GGA functionals. *Organic & biomolecular chemistry*, 9(3), 689-700.
- 45] Shaban, Mohamed & Abdelkarem, Khaled & Sayed, Adel. (2019). Structural, optical and gas sensing properties of Cu₂O/CuO mixed phase: effect of the number of coated layers and (Cr + S) co-Doping. *Phase Transitions*. 92. 1-13.
- 46] A Study on Synthesis and Characterization of Some (I -IV -VI) Groups Compounds for Solar Cells Energy Application for Partial Fulfillment of the Requirements for The Master Degree of science in Chemistry (Physical Chemistry) The Former CMRDI President - Scientific Figure on ResearchGate. Available from: https://www.researchgate.net/figure/Fig-35-Schematic-diagram-of-the-scanning-electron-microscope-SEM_fig5_331989270
- 47] Ghazal, H., & Sohail, N. (2023). Sputtering Deposition. In *Thin Films - Deposition Methods and Applications*. IntechOpen.
- 48] Thickness Measurement of Photoresist Thin Films Using Interferometry - Scientific Figure on ResearchGate. Available from: https://www.researchgate.net/figure/Schematic-representation-of-the-principle-of-operation-of-the-optical-profilometry-for_fig2_221929678
- 49] 6.4 the solar spectrum (no date) 6.4 The Solar Spectrum | METEO 300: Fundamentals of Atmospheric Science. Available at: <https://www.e-education.psu.edu/meteo300/node/683>.
- 50] Rahman, A.S.M.S., Islam, M.A. and Shorowordi, K.M. (2015) 'Electrodeposition and characterization of copper oxide thin films for solar cell applications', *Procedia Engineering*, 105, pp. 679–685. doi:10.1016/j.proeng.2015.05.048.
- 51] AIP Conference Proceedings 2056, 020006 (2018); <https://doi.org/10.1063/1.5084979>